

JGR Biogeosciences

RESEARCH ARTICLE

10.1029/2020JG006158

Khelvi Biriukova and Javier Pacheco-Labrador contributed equally to this work.

Key Points:

- Singular Spectrum Analysis (SSA) allowed to separate slow and fast temporal dynamics in time series of the Photochemical Reflectance Index and apparent fluorescence yield
- SSA successfully extracted the effect of de-epoxidation state of the xanthophyll cycle on leaf absorptance in time series simulated with Soil Canopy Observation of Photochemistry and Energy fluxes model
- SSA allows decoupling long-term biophysical and rapid physiological changes in high temporal resolution spectral measurements

Supporting Information:

Supporting Information may be found in the online version of this article.

Correspondence to:

K. Biriukova,
khelvi.biriukova@gmail.com

Citation:

Biriukova, K., Pacheco-Labrador, J., Migliavacca, M., Mahecha, M. D., Gonzalez-Cascon, R., Martin, M. P., & Rossini, M. (2021). Performance of singular spectrum analysis in separating seasonal and fast physiological dynamics of solar-induced chlorophyll fluorescence and PRI optical signals. *Journal of Geophysical Research: Biogeosciences*, 126, e2020JG006158. <https://doi.org/10.1029/2020JG006158>

Received 6 NOV 2020

Accepted 5 AUG 2021

Author Contributions:

Conceptualization: Khelvi Biriukova, Javier Pacheco-Labrador, Mirco Migliavacca, Miguel D. Mahecha, Micol Rossini

© 2021. The Authors.

This is an open access article under the terms of the [Creative Commons Attribution](https://creativecommons.org/licenses/by/4.0/) License, which permits use, distribution and reproduction in any medium, provided the original work is properly cited.

Performance of Singular Spectrum Analysis in Separating Seasonal and Fast Physiological Dynamics of Solar-Induced Chlorophyll Fluorescence and PRI Optical Signals

Khelvi Biriukova¹ , Javier Pacheco-Labrador² , Mirco Migliavacca^{2,3} , Miguel D. Mahecha^{2,4} , Rosario Gonzalez-Cascon⁵ , M. Pilar Martín⁶ , and Micol Rossini¹ 

¹Remote Sensing of Environmental Dynamics Laboratory, DISAT, University of Milano-Bicocca, Milan, Italy, ²Max Planck Institute for Biogeochemistry, Jena, Germany, ³German Centre for Integrative Biodiversity Research (iDiv) Halle-Jena-Leipzig, Leipzig, Germany, ⁴Remote Sensing Centre for Earth System Research, Leipzig University, Leipzig, Germany, ⁵Department of Environment, National Institute for Agriculture and Food Research and Technology (INIA), Madrid, Spain, ⁶Environmental Remote Sensing and Spectroscopy Laboratory (SpecLab), Spanish National Research Council (CSIC), Madrid, Spain

Abstract High temporal resolution measurements of solar-induced chlorophyll fluorescence (F) and the Photochemical Reflectance Index (PRI) encode vegetation functioning. However, these signals are modulated by time-dependent processes. We tested the applicability of the Singular Spectrum Analysis (SSA) for disentangling fast components (physiology-driven) and slow components (controlled by structural and biochemical properties) from PRI , far-red F (F_{760}), and far-red apparent fluorescence yield (Fy^*_{760}). The proof of concept was developed on spectral and flux time series simulated with the Soil Canopy Observation of Photochemistry and Energy fluxes (SCOPE) model. This allowed the evaluation of SSA decomposition against variables that are independent of physiology or are modified by it. Slow SSA-decomposed components of PRI and Fy^*_{760} showed high correlations with the reference variables ($R^2 = 0.97$ and 0.96 , respectively). Fast SSA-decomposed components of PRI and Fy^*_{760} were better related to the physiological reference variables than the original signals during periods when leaf area index (LAI) was above $1 \text{ m}^2 \text{ m}^{-2}$. The method was also successfully applied to predict light-use efficiency (LUE) from the fast SSA-decomposed components of PRI ($R^2 = 0.70$) and Fy^*_{760} ($R^2 = 0.68$) when discarding data modeled with $LAI < 1 \text{ m}^2 \text{ m}^{-2}$ and short-wave radiation $R_{in} < 250 \text{ W m}^{-2}$. The method was then tested on data acquired in a Mediterranean grassland. In this case, the fast SSA-decomposed component of apparent LUE^* showed a stronger correlation with the fast SSA-decomposed component of Fy^*_{760} ($R^2 = 0.42$) than with original Fy^*_{760} ($R^2 = 0.01$). SSA-based approach is a promising tool for decoupling physiological information from measurements acquired with automated proximal sensing systems.

Plain Language Summary A fraction of the solar light, which is absorbed by leaves but is not used during photosynthesis, is released through heat or as chlorophyll fluorescence (F), a small emission of energy. Recently, it became possible to indirectly estimate the heat and F by measuring the solar light incoming and reflected from leaves using high-resolution optical instruments. Heat release can be monitored with the Photochemical Reflectance Index (PRI). While both PRI and F are theoretically linked to the processes associated with photosynthesis, there is a need to remove the disturbing effects from these signals. We tested whether the Singular Spectrum Analysis (SSA) method can identify at which temporal scale (e.g., seasonal, diurnal) physiological processes (i.e., photosynthesis) and vegetation biophysical changes (e.g., phenology) drive variability in PRI and F . We applied the method on artificial time series of PRI and F simulated with a model (Soil Canopy Observation of Photochemistry and Energy fluxes [SCOPE]) and found that SSA can successfully split these signals into several components recognized as slow (seasonally changing structure and pigments) and fast (physiological response to stress) processes. The method was also tested on time series collected in a Mediterranean grassland, yielding promising results in detecting physiologically driven changes in apparent fluorescence yield (F normalized by photosynthetically active radiation).

Data curation: Khelvi Biriukova, Javier Pacheco-Labrador, Rosario Gonzalez-Cascon, M. Pilar Martín
Formal analysis: Khelvi Biriukova, Javier Pacheco-Labrador
Funding acquisition: Mirco Migliavacca, Miguel D. Mahecha, M. Pilar Martín, Micol Rossini
Investigation: Khelvi Biriukova, Javier Pacheco-Labrador, Rosario Gonzalez-Cascon, M. Pilar Martín
Methodology: Khelvi Biriukova, Javier Pacheco-Labrador, Mirco Migliavacca, Miguel D. Mahecha, Micol Rossini
Project Administration: Mirco Migliavacca, Miguel D. Mahecha, Micol Rossini
Software: Khelvi Biriukova, Javier Pacheco-Labrador
Supervision: Mirco Migliavacca, Miguel D. Mahecha, Micol Rossini
Visualization: Khelvi Biriukova
Writing – original draft: Khelvi Biriukova, Javier Pacheco-Labrador
Writing – review & editing: Khelvi Biriukova, Javier Pacheco-Labrador, Mirco Migliavacca, Miguel D. Mahecha, Rosario Gonzalez-Cascon, M. Pilar Martín, Micol Rossini

1. Introduction

Remote and proximal sensing of vegetation are powerful tools for the exploitation of subtle signals related to plant physiology and photosynthesis. During the last two decades, the interest of the remote sensing community toward solar-induced chlorophyll fluorescence (F) and the Photochemical Reflectance Index (PRI) (Gamon et al., 1992) has increased due to evidence of the close relationship between plant physiological properties and these optical signals (Garbulsky et al., 2011; Meroni et al., 2009; Mohammed et al., 2019). A combination of different processes maintains plants' ability to deal with varying environmental conditions and stress factors. Under optimal light conditions and adequate water and nutrients supply, photochemical reactions, including CO_2 assimilation and electron transport, occur at high efficiency. However, when absorbed solar energy exceeds photosynthetic capacity, it risks damaging the reaction centers of the photosystems and must be emitted as F in the 650–850 nm spectral range or dissipated as heat as part of the non-photochemical quenching (NPQ) (Demmig-Adams & Adams, 1992). Since all three mechanisms (carbon-fixation, F and NPQ) compete for the same absorbed energy, the characterization of both F and NPQ might enable accurate inference of photosynthesis from optical signals (Frankenberg & Berry, 2018; Porcar-Castell et al., 2014). One of the NPQ thermal dissipation mechanisms is the de-epoxidation of the xanthophyll cycle pigments (Demmig-Adams, 1990; Niyogi et al., 1997). The excess energy leads to the interconversion of the xanthophyll cycle pigments, violaxanthin to antheraxanthin and then to zeaxanthin, providing a sink for this energy (Demmig-Adams & Adams, 1996; Pfündel & Bilger, 1994; Yamamoto, 1979). This process is quickly reversible, and zeaxanthin is converted back to violaxanthin under low light conditions and during the night. These conversions result in changes of leaf absorptance around 531 nm, which are detectable with PRI (Gamon et al., 1992; Garbulsky et al., 2011).

Based on the conceptual light-use efficiency framework introduced in Monteith (1972), gross primary production (GPP) is the product of the photosynthetically active radiation (PAR) absorbed by chlorophyll ($aPAR_{Cab}$) and the efficiency with which absorbed light can be used to fix atmospheric CO_2 (light-use efficiency, LUE):

$$GPP = aPAR_{Cab} \cdot LUE, \quad (1)$$

$aPAR_{Cab}$ is often expressed as a fraction of incoming PAR ($faPAR_{Cab}$), which represents a vegetation property independent of the magnitude of the incoming PAR .

Numerous studies have shown that F and PRI measured from a variety of tower-based (e.g., Cogliati et al., 2015; Kim et al., 2021; Wieneke et al., 2018; Xu et al., 2021), airborne (e.g., Middleton et al., 2017; Rascher et al., 2015; Rossini et al., 2015; Siegmann et al., 2021; Tagliabue et al., 2019), and spaceborne platforms (e.g., Middleton et al., 2016; Sun et al., 2018; Wang et al., 2020; Zhang et al., 2020) can successfully track variations in GPP and/or LUE . However, canopy-scale F and PRI are not exclusively driven by plant physiology. Structural and biochemical properties of vegetation varying at different timescales also affect F and PRI signals remotely observed. Phenological changes in pigment pools and canopy structure (e.g., leaf area index, LAI) induce a slow variation of these signals. Faster changes take place at diurnal scales driven by directional effects (sun position and illumination conditions) and physiological responses to environmental and stress conditions (e.g., high vapor pressure deficit, VPD).

At seasonal scale, PRI is sensitive to leaf properties, especially to slow pigment pool modifications responding to environmental factors such as sun exposure, aging, or chronic stress (Filella et al., 2009). These irreversible changes are termed constitutive components of PRI (Gamon & Berry, 2012). Facultative PRI components lead to fast and reversible physiological variations related to the de-epoxidation state (DEPS) of xanthophylls in response to illumination intensity (Demmig-Adams & Adams, 1992).

Following the adaptation of the LUE model proposed by Lee et al. (2013) top of the canopy (TOC) F signal can be defined as:

$$F = aPAR_{Cab} \cdot \phi_f \cdot f_{esc}, \quad (2)$$

where ϕ_f is the physiological F emission yield and f_{esc} is the fraction of all F photons that escape from the canopy. Both $faPAR_{Cab}$ and f_{esc} are controlled by canopy structure and leaf biochemical properties (Martini et al., 2019; Migliavacca et al., 2017), which usually vary at seasonal timescales. Fluorescence yield ϕ_f in

turn, directly responds to the energy partitioning in the photosynthetic machinery. Therefore, it represents a short-term variability (diurnal and sub-diurnal) driven by the modulation of the physiological status of plants.

The recent development of coupled photosynthesis and radiative transfer models (RTMs) (e.g., the Soil Canopy Observation of Photochemistry and Energy fluxes, SCOPE (van der Tol et al., 2009)), able to simulate physiologically driven F and PRI (Vilfan et al., 2018), allowed a better characterization of the physiological and biophysical components of these optical signals. However, the separation of the physiological and radiative sources of variability in long-term measurements of reflectance and F is still a challenge. This knowledge gap hampers the full exploitation of long-term data series collected by unattended spectroradiometric systems, such as those described in Porcar-Castell et al. (2015).

Alternatively, statistical approaches have been successfully used to decompose overlapping signals. For example, the Singular Spectrum Analysis (SSA) is a comprehensive methodology originally established by Broomhead and King (1986) and Fraedrich (1986) and later developed by Ghil et al. (2002) and Golyandina et al. (2001). SSA is a powerful tool for decomposition, reconstruction, and forecasting of climatic time series (Ghil et al., 2002; Plaut et al., 1995; Yiou et al., 1996). Also, SSA was successfully used for the characterization of the dynamics of eddy covariance (EC) ecosystem-atmosphere fluxes (Mahecha et al., 2007; Mahecha, Reichstein, Jung, et al., 2010; Wang et al., 2012) and for the evaluation of terrestrial biosphere and semi-empirical model performances at different timescales (Mahecha, Reichstein, Carvalhais, et al., 2010; Migliavacca et al., 2015). The main idea behind SSA is that time series can be described as a sum of superimposed subsignals, which can be extracted based on their characteristic scales of variability (Mahecha, Reichstein, Jung, et al., 2010). Unlike other methods, one-dimensional SSA is non-parametric, and therefore, it does not require prior information about the number and/or frequencies of periodicities, nor a model for trend (Golyandina et al., 2018).

In this work, we extend the use of SSA to decompose time series of optical signals related to the photosynthetic activity of plants, such as PRI , far-red fluorescence (F_{760}), and far-red apparent fluorescence yield ($Fy_{760}^* = F_{760}/PAR$). We hypothesize that SSA can coherently decouple fast and slow components of the variability of these signals. We test this hypothesis by evaluating to what extent SSA fast components can be attributed to vegetation's physiological responses and SSA slow components to seasonal variations of structural and biochemical properties. We also evaluate the potential of SSA fast components to predict NPQ and LUE . First, we tested SSA on time series of half-hourly data simulated with the state-of-the-art model SCOPE. Then, we applied SSA to automated proximal sensing and EC time series acquired in a Mediterranean grassland.

2. Methods

2.1. SCOPE Simulations

SCOPE version 1.73 was used to simulate one year of TOC reflectance factors (R), F , and fluxes at half-hourly time steps (Biriukova et al., 2021). Variations of leaf absorptance between 500 and 570 nm induced by the inter-conversions of the xanthophyll cycle pigments were simulated by the leaf RTM Fluspect (Fluspect-CX) (Vilfan et al., 2018). Fluorescence radiance was simulated by SCOPE using the fluorescence emission spectra characterized from the FluoWat leaf clip measurements (fluorescence of photosystems I and II are not separated, SCOPE parameter “calc_PSI” = 0) (Vilfan et al., 2016) and an empirical fluorescence model (van der Tol et al., 2014) (SCOPE parameter “Fluorescence_model” = 0).

The distribution of absorbed light into competitive pathways is controlled by the rate coefficients (K), which express the probability of the different fates of the excitations (van der Tol et al., 2014). The rate constant for constitutive thermal dissipation that is present in dark-adapted plants (K_d) was defined as a function of leaf temperature (T) as $K_d = \max(0.8738, 0.0301 \cdot (T - 273.15) + 0.0773)$. The rate constant for fluorescence (K_f) was set to 0.05, and the rate constant for heat dissipation as part of NPQ (K_n) was defined as $K_n = K_{no} \cdot (1 + \beta) \cdot x^\alpha / (\beta + x^\alpha)$, where K_{no} , α , and β are parameters of the empirical model (equal to 5.01, 1.93, 10, respectively). The rate constant of photochemistry (K_p) was set to 4. The degree of light saturation (x , used for computation of K_n), the steady-state fluorescence yield (F_s), and the fluorescence efficiency amplification factor (ϕ'_f) are the output parameters of SCOPE's fluorescence model. NPQ was computed as $K_n/(K_f + K_d)$.

The steady-state fluorescence yield was computed as $F_s = F_m \cdot (1 - \phi_p)$, where light-adapted fluorescence yield is $F_m = K_f / (K_f + K_d + K_n)$, and the photochemical yield is $\phi_p = \phi_p^0 \cdot J_a / J_e$; where ϕ_p^0 is the photochemical yield under dark-adapted conditions, J_a is the actual electron transport rate, and J_e is the potential electron transport rate (van der Tol et al., 2014).

The simulations included temperature correction of the maximum carboxylation rate (V_{cmax} , [$\mu\text{mol m}^{-2} \text{s}^{-1}$]) (SCOPE parameter “apply_T_corr” = 1). Soil heat flux was defined as a constant fraction of soil net radiation (SCOPE parameter “soil_heat_method” = 2).

SCOPE was parameterized to reproduce the spectral behavior of a Mediterranean grassland using vegetation properties derived from field measurements, as well as meteorological data from the research station of Majadas de Tiétar (39°56′24.68″N, 5°45′50.27″W) (Cáceres, Spain). The station is located in a typical Mediterranean savanna ecosystem dominated by herbaceous stratum constituted by grasses, forbs, and legumes. The site is characterized by a mean annual temperature of 16°C but a strong seasonality encompassing a wet season from November to May and dry summers (Perez-Priego et al., 2015). A complete description of the study site can be found in El-Madany et al. (2018) and Perez-Priego et al. (2017).

In order to realistically represent seasonal and intra-daily meteorological conditions, we used half-hourly observations of forcing meteorological variables measured in 2016 (Perez-Priego et al., 2017). Down-welling short wave (R_{in} , [W m^{-2}]) and long wave (R_{lb} , [W m^{-2}]) radiation, air temperature (T_{air} , [°C]), atmospheric vapor pressure (e_a , [hPa]), air pressure (p , [hPa]), relative humidity (RH , [%]), and wind speed (u , [m s^{-1}]) were recorded at 1.6 m height. VPD , [hPa] was computed from T_{air} , e_a , and RH . Sun zenith (SZA , [°]) and azimuth (SAA , [°]) angles were computed from site coordinates and timestamps using the algorithm of Reda & Andreas, 2004.

Soil moisture content (SM_p , [%]) averaged from 4 sensors at 5 cm depth was used to modulate soil R in the brightness-shape-moisture (BSM) sub-model of SCOPE (Verhoef et al., 2018). The parameterization of SCOPE was defined according to Pacheco-Labrador et al. (2019) in the same site. Soil resistance for evaporation from the pore space (r_{ss} , [s m^{-1}]) was estimated from SM_p as in Pacheco-Labrador et al. (2019).

Seasonal variability of LAI [$\text{m}^2 \text{m}^{-2}$], leaf chlorophyll (C_{ab} , [$\mu\text{g cm}^{-2}$]) and carotenoid contents (C_{ca} , [$\mu\text{g cm}^{-2}$]) was simulated from time series of midday Normalized Difference Vegetation Index ($NDVI$) (Tucker, 1979) measured in 2016 by Decagon SRS sensor (Decagon Devices, Pullman, WA) at the study site (Luo et al., 2018). Therefore, these parameters varied daily. LAI was derived from an empirical relationship with $NDVI$ (Martín et al., 2020) (roughly three times $NDVI$). C_{ab} was predicted using a model fit from field spectral measurements and pigment content determined from destructive samples of 25 × 25 cm grass patches, sampled in several campaigns between 2017 and 2019 (Martín et al., 2020; Melendo-Vega et al., 2018). C_{ab} was estimated as $C_{ab} = (0.007 - (0.0001/NDVI) \cdot \log(1 + (NDVI/0.0001))) \cdot 4,443$, while C_{ca} was predicted as a function of C_{ab} , according to the linear model $C_{ca} = 0.24 \cdot C_{ab} + 0.67$ using field information from the same data set. The ratio of C_{ab} to C_{ca} of the simulated data set ranged from 3.06 in autumn to 3.78 in spring. Other parameters were kept constant during the simulation. Leaf angle distribution was assumed spherical, V_{cmax} was set to 80 $\mu\text{mol m}^{-2} \text{s}^{-1}$, and the slope (m , [-]) of the Ball-Berry model (Collatz et al., 1991) was set to 10. These parameters were fixed to simplify the simulations. A constant diffuse to global radiation ratio was set to 20%. Moreover, the variables from the biochemical model of SCOPE (e.g., NPQ , ϕ'_f , ϕ_p), which are not part of the default output of SCOPE, were also extracted. The same way as the model fluxes (e.g., GPP), these variables were computed as a weighted mean of all leaves inside the canopy, considering leaf angle distribution and the relative depth of each leaf, which determine the amount of radiation that each leaf receives (van der Tol et al., 2009). However, unlike the fluxes, biochemical variables were not scaled by LAI since they are leaf rather than canopy scale parameters.

PRI was computed as follows (Gamon et al., 1992):

$$PRI = \frac{R_{570} - R_{531}}{R_{570} + R_{531}} \quad (3)$$

where R_{531} is the reflectance factor of the xanthophyll-sensitive band at 531 nm and R_{570} is the reflectance factor of the reference band at 570 nm. With this formulation, PRI values can vary between -1 and 1 and are directly proportional to NPQ .

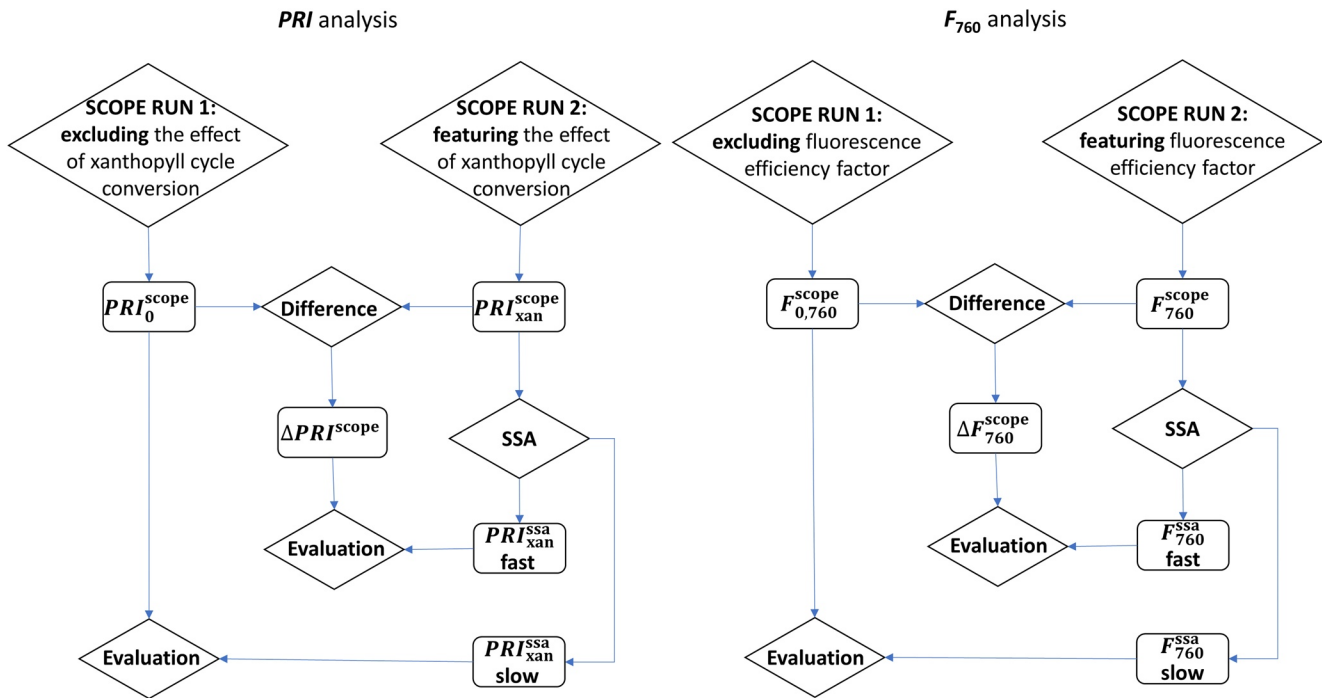


Figure 1. Schematic diagram showing two different runs of Soil Canopy Observation of Photochemistry and Energy fluxes (SCOPE) model and the workflow of Singular Spectrum Analysis (SSA) decomposition.

To evaluate whether extracted SSA components were related either to the constitutive or the facultative drivers of variability, SCOPE model was run in two different modes featuring and excluding physiological effects on PRI and F (i.e., the effect of the xanthophyll cycle de-epoxidation on leaf absorption and fluorescence efficiency amplification factor (ϕ'_f) on F). PRI_{xan}^{scope} was simulated featuring the effect of changes in the DEPS of the xanthophyll cycle pigments on leaf absorptance with Fluspect-CX (Vilfan et al., 2018), whereas PRI_0^{scope} was computed from R where the effect of the conversion of violaxanthin into zeaxanthin in the xanthophyll cycle was not simulated (Figure 1). Therefore, ΔPRI^{scope} , computed as the difference between PRI_{xan}^{scope} and PRI_0^{scope} , expresses PRI variability induced only by physiological changes.

Similarly, we simulated a baseline TOC fluorescence featuring (F_{760}^{scope}) and excluding ϕ'_f modulation ($F_{0,760}^{scope}$) predicted by the photosynthesis-fluorescence model of SCOPE (van der Tol et al., 2014) (Figure 1). Baseline fluorescence corresponds to the emission under unstressed, low light conditions, only affected by canopy biophysical properties and illumination conditions, while the difference between F_{760}^{scope} and $F_{0,760}^{scope}$ (ΔF_{760}^{scope}) expresses the physiological regulation of fluorescence emission.

The corresponding apparent fluorescence yield variables (Fy_{760}^{*scope} , $Fy_{0,760}^{*scope}$) were computed as F normalized by PAR . We used PAR instead of $aPAR_{Cab}$ since the second is not directly measured in most ecosystem stations. Therefore, we normalized F with PAR to test the SSA's applicability on the variable most often available. The ratio $\Delta F_{760}^{scope}/PAR$ was computed to validate the SSA-decomposed physiology-related component of Fy_{760}^{*scope} . For the definition of the variables simulated with SCOPE and modeled with SSA refer to Table 1.

Only daytime data were simulated. Any situation where $R_{in} \leq 10 \text{ W m}^{-2}$ or $SZA \geq 85^\circ$ was considered night. Night-time values of different model outputs were linearly interpolated between the sunrise and sunset values. However, R could strongly change due to small variations in SZA when it is large. Therefore, sunrise and sunset were simulated differently to provide a smooth baseline. For these time steps, we set $SZA = 85^\circ$ and used the forcing meteorological variables of the following or the previous time step, respectively. R was calculated for $R_{in} = 10 \text{ W m}^{-2}$ using the optical radiative transfer module of SCOPE only so that no physio-

logical effect was present and night-time baselines for both $PRI_{\text{xan}}^{\text{scope}}$ and PRI_0^{scope} were identical. The rest of the model outputs were computed for $R_{\text{in}} = 0 \text{ W m}^{-2}$ using the full model. At such low radiation levels, the effects of the xanthophyll cycle on R resulted negligible, and it was assumed that these simulations could be representative of dark night-time. Night-time interpolation is necessary since SSA requires continuous data. This gap-filling is reasonable for parameters that are not expected to strongly vary during the night, such as F or R -based variables, as is the case for PRI . These assumptions might not completely hold due, for example, to physiological recovery. Since PAR equals 0 at night, the night-time gaps in the series of Fy_{760}^* were filled with the maximum daytime values selected in the moving window of 1 day. We simulated observational uncertainty by adding Gaussian noise to the time series of PRI , F_{760} , and Fy_{760}^* with 0 mean (μ), standard deviation (σ) equal to the 95% quantile of daytime data multiplied by 0.01. LUE [$\mu\text{mol CO}_2/\mu\text{mol photons absorbed}$] was computed as the ratio of simulated GPP to $aPAR_{\text{Cab}}$.

2.2. Singular Spectrum Analysis

SSA is one of several potential time series decomposition techniques. It was chosen here because it is highly data-adaptive and allows for decomposing phase-modulated signals. The method can be described in four steps: embedding, decomposition, grouping, and reconstruction (Golyandina & Korobeynikov, 2014) (Figure 2).

Step 1 Embedding. The original time series $Y = (f_1, \dots, f_N)$ of length N is transformed into a time-delay-embedding covariance matrix composed of a sequence of $K = N - L + 1$ lagged vectors of length L (window length):

$$X_i = (x_i, \dots, x_{i+L-1})^T, i = 1, \dots, K \quad (4)$$

Step 2 Decomposition. Singular value decomposition (SVD) leads to elementary matrices of rank 1:

$$X = X_1 + \dots + X_d \quad (5)$$

where d is a rank of X . Each elementary matrix X_i is defined by the eigentriple:

$$X_i = \sqrt{\lambda_i} U_i V_i^T \quad (6)$$

The eigentriple consists of a singular value $\sqrt{\lambda_i}$, the left eigenvector U_i and the right eigenvector V_i . The singular values of eigentriples are proportional to the fraction of explained variance corresponding to each eigentriple.

Step 3 Grouping. The grouping is performed by choosing the sets of eigentriples (eigentriple grouping) so that each set corresponds to an identifiable series component. The grouping procedure partitions the set of indices $\{1, \dots, d\}$ into m disjoint subsets I_1, \dots, I_m . The result of this step is the grouped matrix decomposition of the expansion (6):

$$X = X_{I_1} + \dots + X_{I_m} \quad (7)$$

Step 4 Reconstruction. In the last step, each matrix of the grouped decomposition (7) is transformed into a new series of length N by diagonal averaging. As a result, the initial time series (f_1, \dots, f_N) is decomposed into a sum of m reconstructed series:

$$f_n = \sum_{k=1}^m \tilde{f}_n^{(k)}, n = 1, \dots, N. \quad (8)$$

Time series decomposition was implemented using R-packages *Rssa* (Golyandina et al., 2018; Korobeynikov et al., 2017) and *spectral.methods* (Buttler et al., 2014). There are two parameters in SSA, which the analyst must set: the window length (L) and grouping of the eigentriples. The choice of L is dependent on the characteristics of the subsignals to be extracted. In general, $L \leq N/2$, and the higher the L , the more detailed the

decomposition is. For the identification of the trend, L should be large enough to be separable from periodic oscillations and noise. For the extraction of a periodic component with a period T , it is advisable to have L proportional to T . The periods of the harmonic components of the time series can be identified with the periodogram.

The grouping can be done manually by analyzing the graphs of eigenvectors and their frequencies or automatically (Golyandina & Zhigljavsky, 2013). In this study, we used the automatic grouping implemented in *spectral.methods* R-package (Buttlar, 2015), which groups SSA components based on their common features. This method measures the commonality of components by means of the weighted correlations between the components: if the weighted correlation is high, then the corresponding components have similar behaviors and should be included in one group (Golyandina et al., 2018).

The whole algorithm was run stepwise for each frequency interval (which are specified by “borders.wl” argument, Table S1). This allows adapting L for a particular frequency bin to be extracted. The choice of frequency bands is subjective and was determined here based on the time series length and temporal resolution (30 min). We divided time series into three intuitive frequency bins to test SSA component extracted in different bins and their relationships with reference signals (i.e., PRI_0^{scope} , $\Delta PRI^{\text{scope}}$, $F_{0,760}^{\text{scope}}$, $\Delta F_{760}^{\text{scope}}$). In particular, we defined the following classes: long-term or seasonal (2 weeks–1 year), diurnal (7 h–2 weeks), sub-diurnal (30 min–7 h). For each frequency bin, the chosen window length L was: 2 months, 1 week, and 1 day. The choice of window length was supported by the SSA theory (i.e., for extracting the long-term component, L was chosen large enough to be separable from the periodic component, while for the extraction of diurnal oscillations, L was proportional to the period of 1 day). The data associated with the output of SSA analysis can be found in Biriukova et al. (2021).

SSA decomposition was applied on time series of $PRI_{\text{can}}^{\text{scope}}$, PRI_0^{scope} , F_{760}^{scope} , $F_{0,760}^{\text{scope}}$, Fy_{760}^{scope} , $Fy_{0,760}^{\text{scope}}$. The parameters of the decomposition used in the function *filterTSeriesSSA* are reported in Table S1.

2.3. Field Data Acquisition and Processing

Spectral measurements (hereafter denoted with subscript “m”) were acquired in Majadas de Tiétar with the high-resolution fluorescence box (FloX) device (JB Hyperspectral Devices UG, Germany), specifically designed for retrieving F and vegetation indices in visible (VIS) and near-infrared (NIR) domains. The FloX system contains two spectrometers — QE Pro (wavelength range of 650–813 nm, spectral sampling interval (SSI) of 0.15 nm and full width at half maximum (FWHM) of 0.3 nm), and Flame (wavelength range of 340–1,020 nm, SSI = 0.65 nm, FWHM = 1.5 nm) (Ocean Optics, USA). The up-welling radiance was measured with the 25° field of view (FOV) of fiber optics. Down-welling irradiance was measured using hemispherical cosine receptors. The FloX was installed on a radiometric tower at 10 m height, which resulted in a radiometric footprint of approximately 4.4 m in diameter. An automatic rotating arm allows sequential measurements over a tree and herbaceous stratum with an interval of 15 min. In this work, we use measurements acquired over the herbaceous stratum only. Measurements were collected continuously from 6 a.m. to 7 p.m. (UTC time) with an average interval of 2 min. The data set covers the period from March 5, 2017 to October 24, 2018, with gaps associated with the instrument’s technical issues from mid-June 2017 to mid-August 2017 and from mid-January 2018 to mid-March 2018.

CO₂ fluxes between vegetation and atmosphere were measured with the EC technique (e.g., Baldocchi et al., 1996) (hereafter denoted with subscript “m”). EC system consists of an infrared gas analyzer LI-COR LI7200 (LI-COR Inc, Lincoln NE) and a three-dimensional sonic anemometer Gill R3-50 (Gill Instruments Ltd., Lymington). EC was installed at the height of 1.6 m to measure the fluxes of the herbaceous stratum (Perez-Priego et al., 2017). Net ecosystem exchange (NEE , [$\mu\text{mol CO}_2 \text{ m}^{-2} \text{ s}^{-1}$]) was partitioned into GPP_m , [$\mu\text{mol CO}_2 \text{ m}^{-2} \text{ s}^{-1}$] and ecosystem respiration ($Reco_m$, [$\mu\text{mol CO}_2 \text{ m}^{-2} \text{ s}^{-1}$]) using nighttime-based method (Reichstein et al., 2005). Apparent LUE_m^* [$\mu\text{mol CO}_2 / \mu\text{mol PAR photons}$] was computed as the ratio of GPP_m to PAR_m .

Spectral data were aggregated in 30 min intervals and matched with fluxes observations. Gap-filling procedure for measured variables (PRI_m , $F_{760,m}$, $Fy_{760,m}^*$, LUE_m^*) included several steps. First, data points acquired

under $SZA > 70^\circ$ were discarded. Second, we applied linear interpolation to fill missing data points for each day that included more than five valid daytime observations. Third, large gaps in the time series were filled using the SSA gap-filling approach implemented in the function *gapfillSSA* of the *spectral.methods* R-package (Buttler et al., 2014). Forth, the night-time baseline was recomputed for each variable by filling it with the maximum or minimum (depending on the variable) daytime values selected in the moving window of 1 day. Last, Gaussian noise was added to night-time baselines with $\mu = 0$ and σ equal to the 95% quantile of daytime data multiplied by 0.01.

Since $aPAR_{Cab}$ was not available from field observations, the apparent LUE_m^* was estimated as the ratio of GPP_m to PAR_m . Light-use efficiency represents a combination of different components - green canopy structure, light absorption, and physiology (Gitelson & Gamon, 2015). For this reason, we applied the SSA decomposition on LUE_m^* to decouple the influence of canopy biochemical and structural properties (i.e., $faPAR_{Cab}$). In this case, we consider the SSA fast varying component extracted from LUE_m^* a proxy of LUE_m .

PRI_m , $F_{760,m}$, $Fy_{760,m}^*$, and LUE_m^* were decomposed into the same frequency classes as the SCOPE-simulated variables (Section 2.2): long-term or seasonal (2 weeks–1 year), diurnal (7 h–2 weeks), sub-diurnal (30 min–7 h). Parameters of the *filterTSeriesSSA* function used for the decomposition are also identical and reported in Table S1.

3. Results

3.1. Seasonal Cycles of SCOPE-Simulated Variables

The Mediterranean climate is characterized by a strong seasonality, driven mainly by radiation and precipitations (e.g., El-Madany et al., 2018). The rainy period occurs during late fall and early spring, and the dry season in summer extends to early fall (Figure 3b). Simulated biophysical parameters, fluxes, and spectral variables are coherent with the typical phenology of the grassland at the site (Luo et al., 2020). According to the models based on *NDVI* observations, during the green-up period from fall to winter, simulated *LAI* and C_{ab} increased from 0.5 to 2.5 $m^2 m^{-2}$ and from 7.5 to 25 $\mu g cm^{-2}$, respectively (Figure 3d). This variability is coherent with expected phenology and with the variability of SM_p (Figure 3b). The peak of the growing season in Majadas de Tiétar occurs in spring (Luo et al., 2020). This is reproduced by simulated *GPP* and F_{760}^{scope} , which featured maximum values at the beginning of May (Figures 3e, 3i and 3j). Early summer is characterized by a dry-down period, a transition to the hottest and driest season where photosynthesis is strongly inhibited by water stress. Summer T_{air} reaches 40°C and *VPD* values of 75 hPa (Figures 3a and 3b), which is also represented in the simulations.

3.2. ΔPRI^{scope} and ΔF_{760}^{scope} as a Function of Vegetation Physiological Response

The difference between total PRI_{xan}^{scope} and constitutive PRI_0^{scope} denoted as ΔPRI^{scope} (Table 1) represents the vegetation's facultative response to environmental conditions (e.g., solar irradiance) occurring at daily or shorter timescales. ΔPRI^{scope} can be considered a reliable proxy of the changing DEPS of the xanthophyll cycle pigments as part of *NPQ*. The SCOPE-simulated weighted average of *NPQ* of all leaves linearly scales with ΔPRI^{scope} at short temporal scales when canopy structural parameters (*LAI*) do not vary significantly (Figures 4a and 4b). The coefficient of determination (R^2) of the linear relationships between ΔPRI^{scope} and *NPQ* computed for classes of *LAI* of equal size varies within a range of 0.75–0.97.

To validate the decomposition of F_{760}^{scope} into components related either to biophysical or physiological properties, we used ΔF_{760}^{scope} , the difference between F_{760}^{scope} and $F_{0,760}^{scope}$, as a reference for the physiological information contained in the fluorescence signal. F_{760}^{scope} is scaled with the fluorescence efficiency factor predicted by the biochemical model according to the way $aPAR_{Cab}$ is split in the photosynthetic machinery. Therefore, ΔF_{760}^{scope} can be attributed to the physiological regulation of fluorescence efficiency (Figures 4c and 4d). R^2 of the linear relationships between ΔF_{760}^{scope} and ϕ'_i computed for classes of *LAI* of equal size varies within a range of 0.73–0.92.

Table 1

Definition of the Variables Simulated With SCOPE and Extracted With SSA

PRI_{xan}^{scope}	Total PRI featuring the effect of the xanthophyll cycle pigment conversion.
PRI_0^{scope}	Constitutive PRI excluding the effect of the xanthophyll cycle pigment conversion.
ΔPRI^{scope}	Facultative PRI - the difference between PRI_{xan}^{scope} and PRI_0^{scope} .
PRI_{xan}^{ssa}	SSA-decomposed components of total PRI_{xan}^{scope} .
F_{760}^{scope}	Far-red F featuring the fluorescence amplification factor (ϕ'_f) modulation.
$F_{0,760}^{scope}$	Far-red F yield excluding the fluorescence amplification factor (ϕ'_f) modulation.
ΔF_{760}^{scope}	The difference between F_{760}^{scope} and $F_{0,760}^{scope}$.
F_{760}^{ssa}	SSA-decomposed components of far-red F_{760}^{scope} .
Fy_{760}^{*scope}	Far-red apparent F yield featuring the fluorescence amplification factor (ϕ'_f) modulation.
$Fy_{0,760}^{*scope}$	Far-red apparent F yield excluding the fluorescence amplification factor (ϕ'_f) modulation.
Fy_{760}^{*ssa}	SSA-decomposed components of far-red Fy_{760}^{*scope} .

For the decomposition analysis, we assume that the scaling of canopy-level parameters ΔPRI^{scope} and ΔF_{760}^{scope} to leaf-level NPQ and ϕ'_f is unnecessary if the relationship between the decomposed SSA components and NPQ or ϕ'_f is evaluated for different LAI classes.

3.3. Proof of Concept: Extraction of Slow Dynamics From PRI_{xan}^{scope} , F_{760}^{scope} , and Fy_{760}^{*scope} With SSA

The slow-varying components of PRI_{xan}^{ssa} (seasonal), F_{760}^{scope} (seasonal) and Fy_{760}^{*ssa} (seasonal) extracted with SSA are shown in Figures 5a–5c. The slow-varying component of PRI_{xan}^{ssa} (seasonal) (Figure 5a) showed a high correlation with PRI_0^{scope} ($R^2 = 0.97$) (Figure 6a). This confirms that SSA was able to distinguish the long-term variability of PRI_{xan}^{scope} induced by seasonally varying structural and biochemical vegetation properties (e.g., LAI or C_{ab}). The SSA extraction of the seasonal component from F_{760}^{scope} (Figure 5b) performed worse in comparison to PRI_{xan}^{scope} , with $R^2 = 0.46$ of the relationship between F_{760}^{ssa} (seasonal) and $F_{0,760}^{ssa}$ (Figure 6b). The decomposition of Fy_{760}^{*scope} allowed to separate the seasonal cycle (Figure 5c) associated with the variability of $faPAR_{Cab}$. A high positive correlation was observed between Fy_{760}^{*ssa} (seasonal) and $Fy_{0,760}^{*scope}$ ($R^2 = 0.96$) (Figure 6c).

3.4. Proof of Concept: Extraction of Fast Variability From PRI_{xan}^{scope} , F_{760}^{scope} , and Fy_{760}^{*scope} With SSA

The fast-varying components of PRI_{xan}^{ssa} (diurnal + sub-diurnal) (Figure 5d) showed a considerably stronger linear relationship with ΔPRI^{scope} ($R^2 = 0.78$, Figure 7b) compared to PRI_{xan}^{scope} ($R^2 = 0.02$, Figure 7a). The same decomposition applied to PRI_0^{scope} results in a non-significant correlation with ΔPRI^{scope} ($R^2 = 0.05$) (Figure S1), confirming that SSA can extract the physiologically relevant information from PRI_{xan}^{ssa} . PRI_{xan}^{ssa} (diurnal + sub-diurnal) related to ΔPRI^{scope} more strongly than PRI_{xan}^{scope} for all LAI classes above $1 \text{ m}^2 \text{ m}^{-2}$ (Figure 7c). Figure 7c also evaluates the effect of observational uncertainties by presenting the performance of SSA decomposition on noiseless PRI data (dashed lines). As can be seen, the presence of noise does not reduce the capability of PRI_{xan}^{ssa} (diurnal + sub-diurnal) to predict ΔPRI^{scope} (Figure 7c). This supports the hypothesis that SSA can be useful for separating the fast variability of PRI attributed to the activation of the xanthophyll cycle as part of the reversible NPQ .

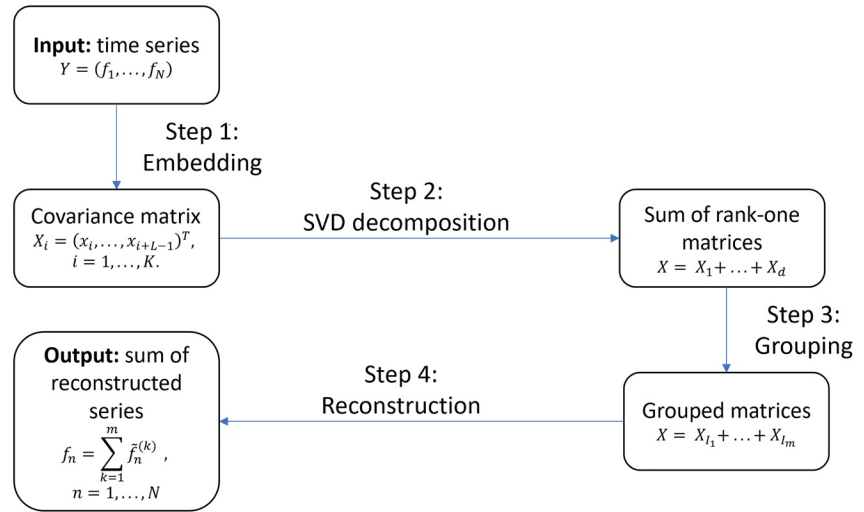


Figure 2. Generic scheme of Singular Spectrum Analysis. Singular value decomposition (SVD) is singular value decomposition.

The fast SSA component F_{760}^{ssa} (diurnal + sub-diurnal) (Figure 7e) showed significant correlations with ΔF_{760}^{scope} for LAI from 1.4 to 2.2 $\text{m}^2 \text{m}^{-2}$, with R^2 ranging from 0.27 to 0.65 (Figure 7f). However, F_{760}^{ssa} (diurnal + sub-diurnal) does not provide more accurate predictions of ΔF_{760}^{scope} than F_{760}^{scope} (Figures 7d–7f). The same results are found for noiseless simulations, which suggest that SSA cannot extract ΔF_{760}^{scope} from F_{760}^{scope} time series.

The fast component of Fy_{760}^{*ssa} (diurnal + sub-diurnal) linearly scales with $\Delta F_{760}^{scope} / PAR$ both for the entire data set ($R^2 = 0.63$, Figure 7h) and for groups of similar LAI (Figure 7i). However, the correlation between $\Delta F_{760}^{scope} / PAR$ and Fy_{760}^{*ssa} is slightly stronger for the whole data set ($R^2 = 0.71$, Figure 7g).

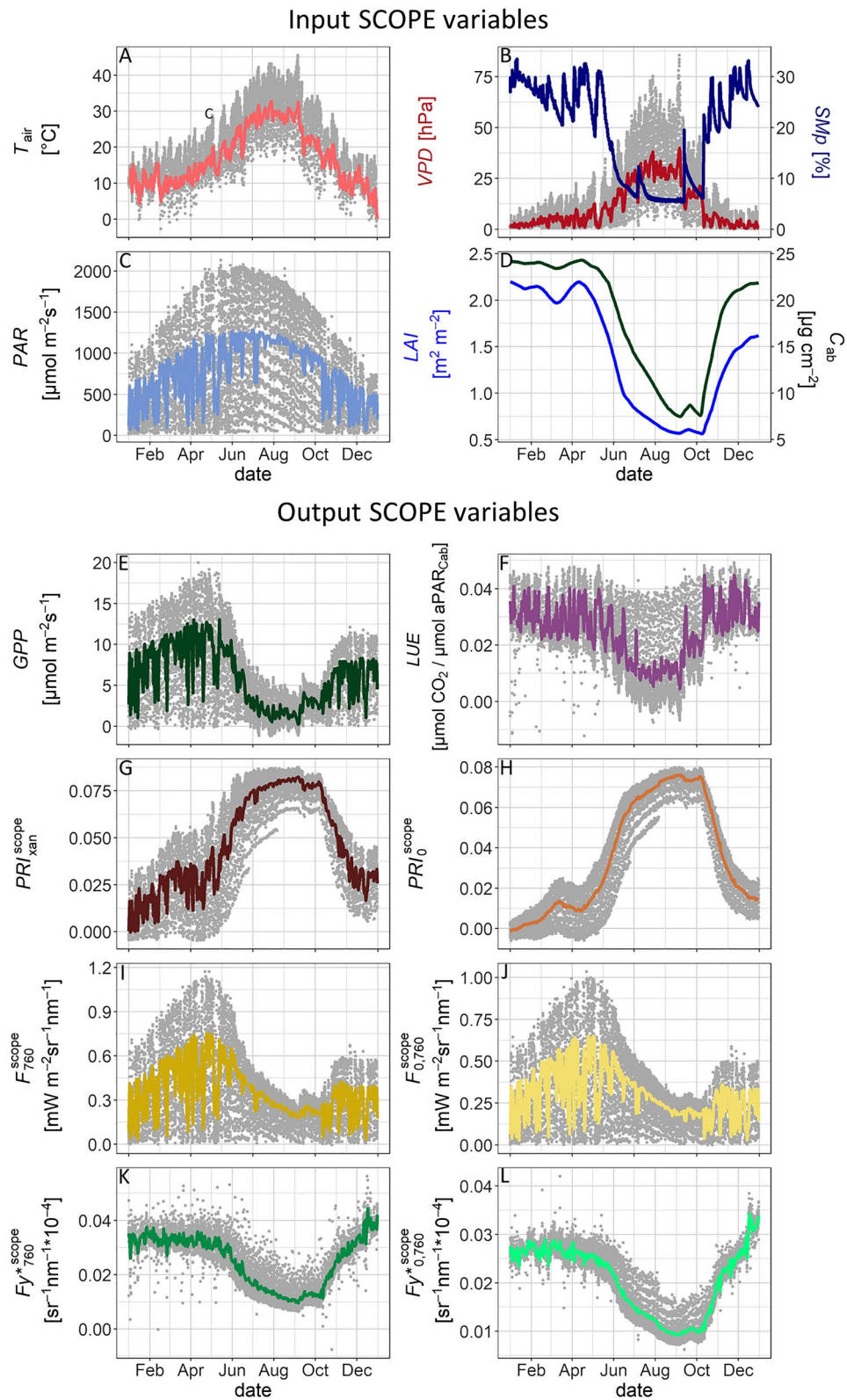
When the comparison is carried out per LAI bins, Fy_{760}^{*ssa} (diurnal + sub-diurnal) cast larger R^2 than Fy_{760}^{*ssa} for LAI > 1.4 $\text{m}^2 \text{m}^{-2}$. The comparison with the decomposition of noiseless data reveals that SSA-decomposed Fy_{760}^{*ssa} (diurnal + sub-diurnal) has a large potential to track $\Delta F_{760}^{scope} / PAR$ better than Fy_{760}^{*scope} ($R^2 > 0.75$), but that it is reduced by the presence of noise in the signal (Figure 7i). To ascertain that Fy_{760}^{*ssa} (diurnal + sub-diurnal) is related to vegetation physiology, we applied the same SSA decomposition to $Fy_{0.760}^{*scope}$. In this case, the components of the same frequency showed a lower correlation with $\Delta F_{760}^{scope} / PAR$ ($R^2=0.48$), but the relationship was still significant (Figure S1).

3.5. Link Between Fast SSA Components of PRI_{xan}^{ssa} and Fy_{760}^{*ssa} and Light-Use Efficiency — Model-Based Scenario

To evaluate whether SSA-decomposed fast components of optical signals are better related to the physiological response of vegetation than the original undecomposed variables, we compared their relationships with LUE (Figure 8). Also, according to the results presented in Figures 7c, 7f and 7i, we considered the limitations of SSA to predict fast components of different spectral variables at low LAI values and evaluated the relationships for data with LAI above 1 $\text{m}^2 \text{m}^{-2}$ (Figure 9).

The fast component PRI_{xan}^{ssa} (diurnal + sub-diurnal) correlated linearly with LUE better than PRI_{xan}^{scope} for LAI > 1.4 $\text{m}^2 \text{m}^{-2}$ (Figure 8g). When we consider only the LAI space where ΔPRI_{xan}^{scope} can be accurately predicted by SSA (i.e., LAI > 1 $\text{m}^2 \text{m}^{-2}$), the overall relationship PRI_{xan}^{ssa} (diurnal + sub-diurnal) versus LUE strongly improves yielding $R^2 = 0.7$ (Figure 9e).

A priori, the decoupling of the Fy_{760}^{*ssa} (diurnal + sub-diurnal) component from Fy_{760}^{*scope} did not improve the relationship with LUE (Figure 8f). When LAI < 1 $\text{m}^2 \text{m}^{-2}$ fast Fy_{760}^{*ssa} (diurnal + sub-diurnal) predicts LUE



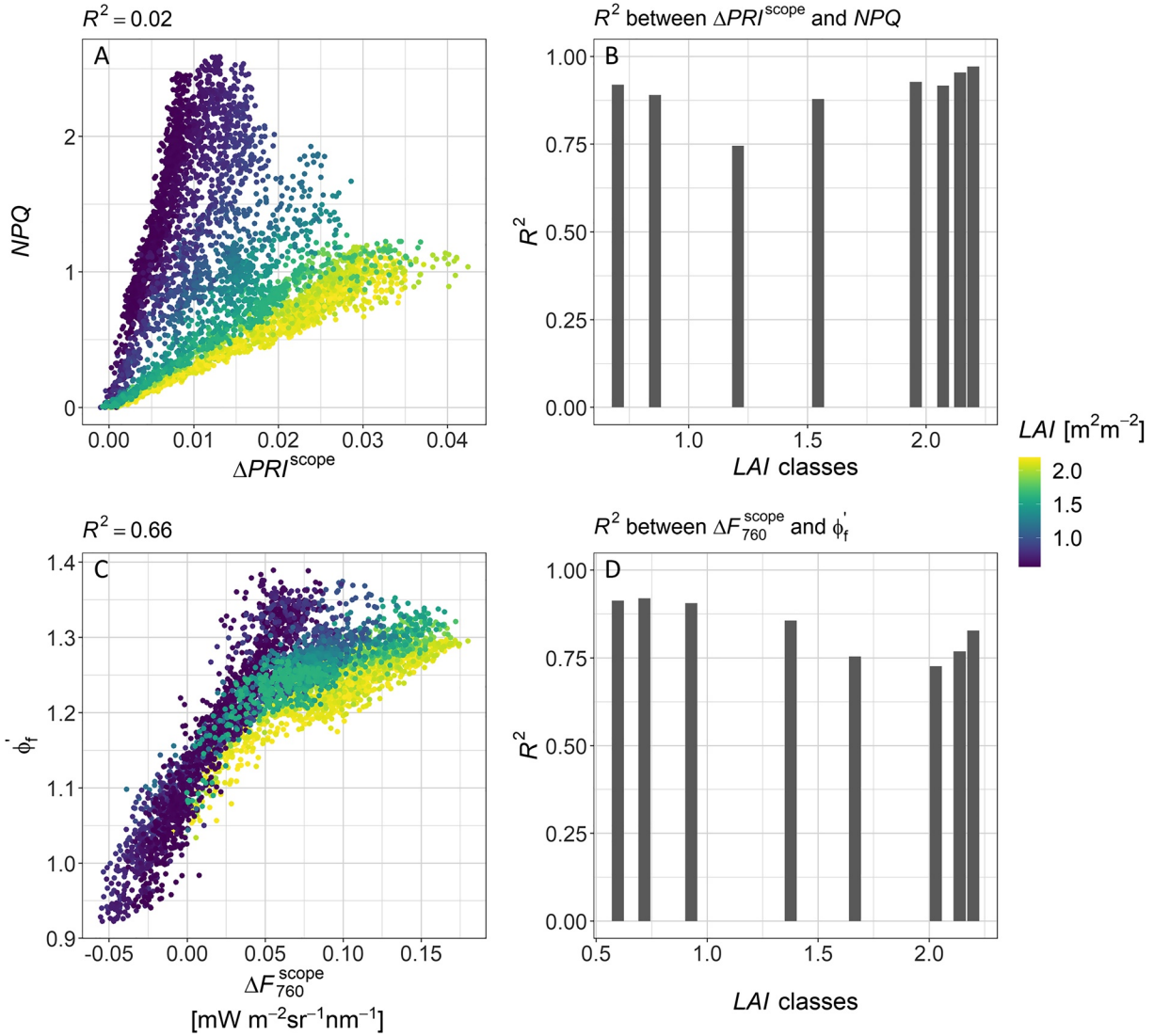


Figure 4. (a) Relationship between $\Delta PRI^{\text{scope}}$ and non-photochemical quenching (NPQ) and (b) coefficients of determination (R^2) for linear relationships between $\Delta PRI^{\text{scope}}$ and NPQ aggregated by leaf area index (LAI) classes of equal size. (c) Relationship between $\Delta F_{760}^{\text{scope}}$ and ϕ'_f and (d) coefficients of determination (R^2) for linear relationships between $\Delta F_{760}^{\text{scope}}$ and ϕ'_f aggregated by LAI classes of equal size. The data presented in the figure correspond to daytime, $SZA \leq 80^\circ$ and the fraction of the day between 0.2 and 0.8.

worse than original signal $Fy_{760}^{*\text{scope}}$ (Figure 8h). Additionally, these relationships are different for high and low light conditions (and, therefore, low NPQ), which makes unsuitable the evaluation of the linear models. When $NPQ < 0.1$ (which in the simulation occurs when $R_{in} < 250 \text{ W m}^{-2}$), the relationship between $Fy_{760}^{*\text{ssa}}$ (diurnal + sub-diurnal) and $\Delta F_{760}^{\text{scope}} / PAR$ and LUE becomes negative (Figure S2). In order to properly evaluate these relationships, we limited the analysis to the cases where $\Delta F_{760}^{\text{scope}} / PAR$ could be acceptably

Figure 3. Time series of input Soil Canopy Observation of Photochemistry and Energy fluxes (SCOPE) model variables: (a) air temperature (T_{air}), (b) vapor pressure deficit (VPD) and soil moisture content (SM_p), (c) photosynthetically active radiation (PAR), (d) leaf area index (LAI) and chlorophyll content (C_{ab}); output SCOPE variables: (e) gross primary production (GPP), (f) light-use efficiency (LUE), (g and h) photochemical reflectance index featuring and excluding the effect of the xanthophyll cycle de-epoxidation ($PRI_{\text{xan}}^{\text{scope}}, PRI_0^{\text{scope}}$), (i and j) far-red fluorescence featuring and excluding fluorescence amplification factor ϕ'_f ($F_{760}^{\text{scope}}, F_{0,760}^{\text{scope}}$), (k and l) far-red apparent fluorescence yield featuring and excluding fluorescence amplification factor ($Fy_{760}^{*\text{scope}}, Fy_{0,760}^{*\text{scope}}$). Gray dots represent the half-hourly values, color lines represent mean daily values for T_{air}, VPD and mean daytime ($SZA \leq 80^\circ$ and the fraction of the day between 0.2 and 0.8) daily values of $PAR, GPP, LUE, PRI_{\text{xan}}^{\text{scope}}, PRI_0^{\text{scope}}, F_{760}^{\text{scope}}, F_{0,760}^{\text{scope}}, Fy_{760}^{*\text{scope}}, Fy_{0,760}^{*\text{scope}}$.

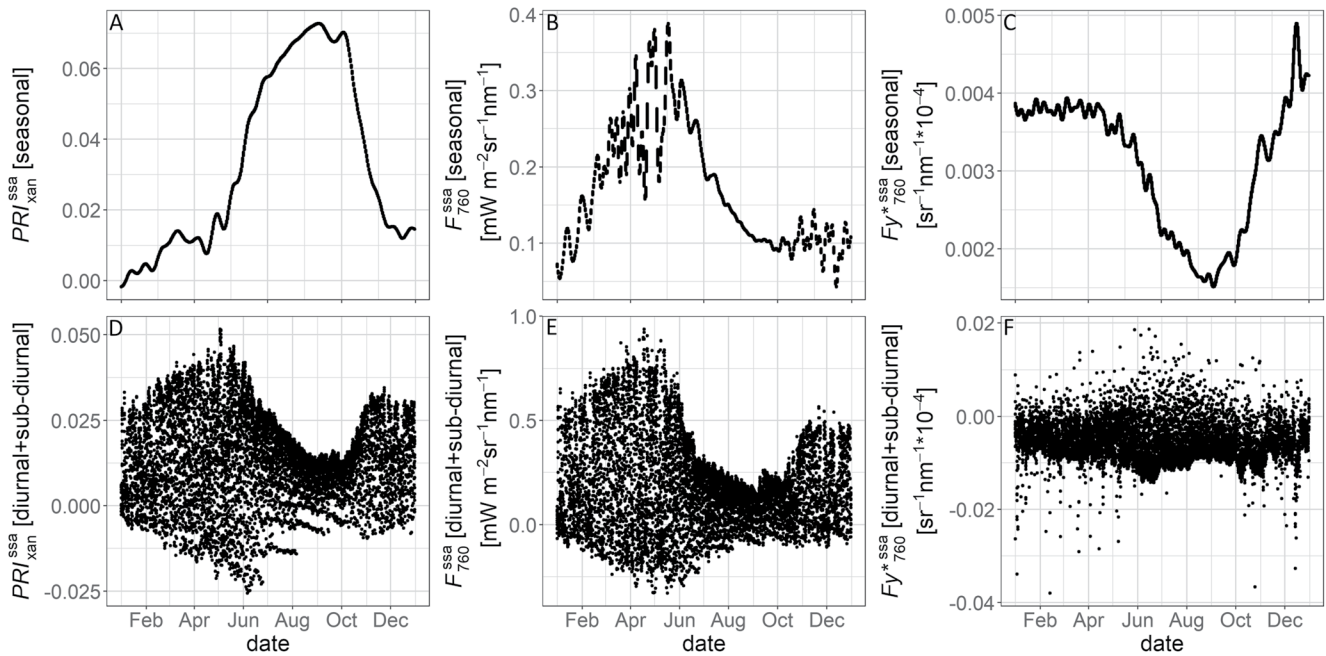


Figure 5. Upper panel: time series of slow varying (seasonal) components extracted with Singular Spectrum Analysis (SSA) - (a) PRI_{xan}^{ssa} (seasonal), (b) F_{760}^{scope} (seasonal), and (c) Fy_{760}^{*ssa} (seasonal). Lower panel: time series of SSA-extracted fast varying (diurnal + sub-diurnal) components - (d) PRI_{xan}^{ssa} (diurnal + sub-diurnal), (e) F_{760}^{ssa} (diurnal + sub-diurnal), and (f) Fy_{760}^{*ssa} (diurnal + sub-diurnal). The data presented in the figure correspond to daytime.

predicted, and the relationships with LUE could be represented by a linear model. Discarding the cases where $LAI < 1 \text{ m}^2 \text{ m}^{-2}$ and $R_{in} < 250 \text{ W m}^{-2}$ (Figures 9b, 9d, 9f and 9h) largely improved the relationship between Fy_{760}^{*ssa} (diurnal + sub-diurnal) and LUE ($R^2 = 0.68$) and reduced the Root Mean Square Error ($RMSE$) both in the Fy_{760}^{*ssa} and the Fy_{760}^{*scope} models (Figures 9b and 9f).

3.6. Link Between Fast SSA Components of PRI_m^{ssa} , $F_{760,m}^{ssa}$, $Fy_{760,m}^{*ssa}$, and LUE_m^{*ssa} — Scenario Based on Real Data

Diurnal and sub-diurnal components of PRI_m^{ssa} , $F_{760,m}^{ssa}$, $Fy_{760,m}^{*ssa}$, and LUE_m^{*ssa} were summed up and considered together as the fast component. We evaluated the relationships between the fast components of PRI_m^{ssa} , $F_{760,m}^{ssa}$, $Fy_{760,m}^{*ssa}$ and the fast component of LUE_m^{*ssa} to assess whether SSA-decomposed spectral variables

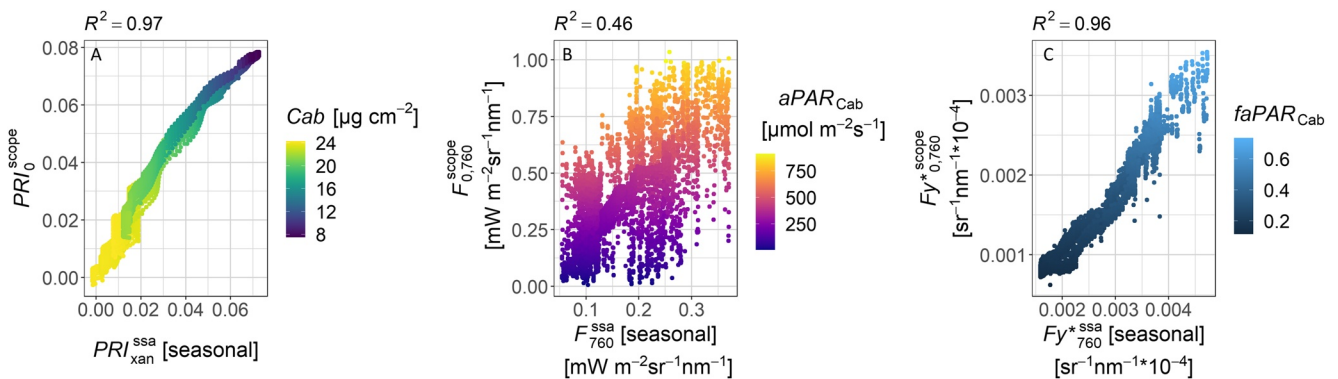


Figure 6. (a) Relationship between PRI_{xan}^{ssa} (seasonal) and PRI_{xan}^{scope} , (b) F_{760}^{ssa} (seasonal) and F_{760}^{scope} , and (c) Fy_{760}^{*ssa} (seasonal) and Fy_{760}^{*scope} . The data presented in the figure correspond to daytime, $SZA \leq 80^\circ$ and the fraction of the day between 0.2 and 0.8.

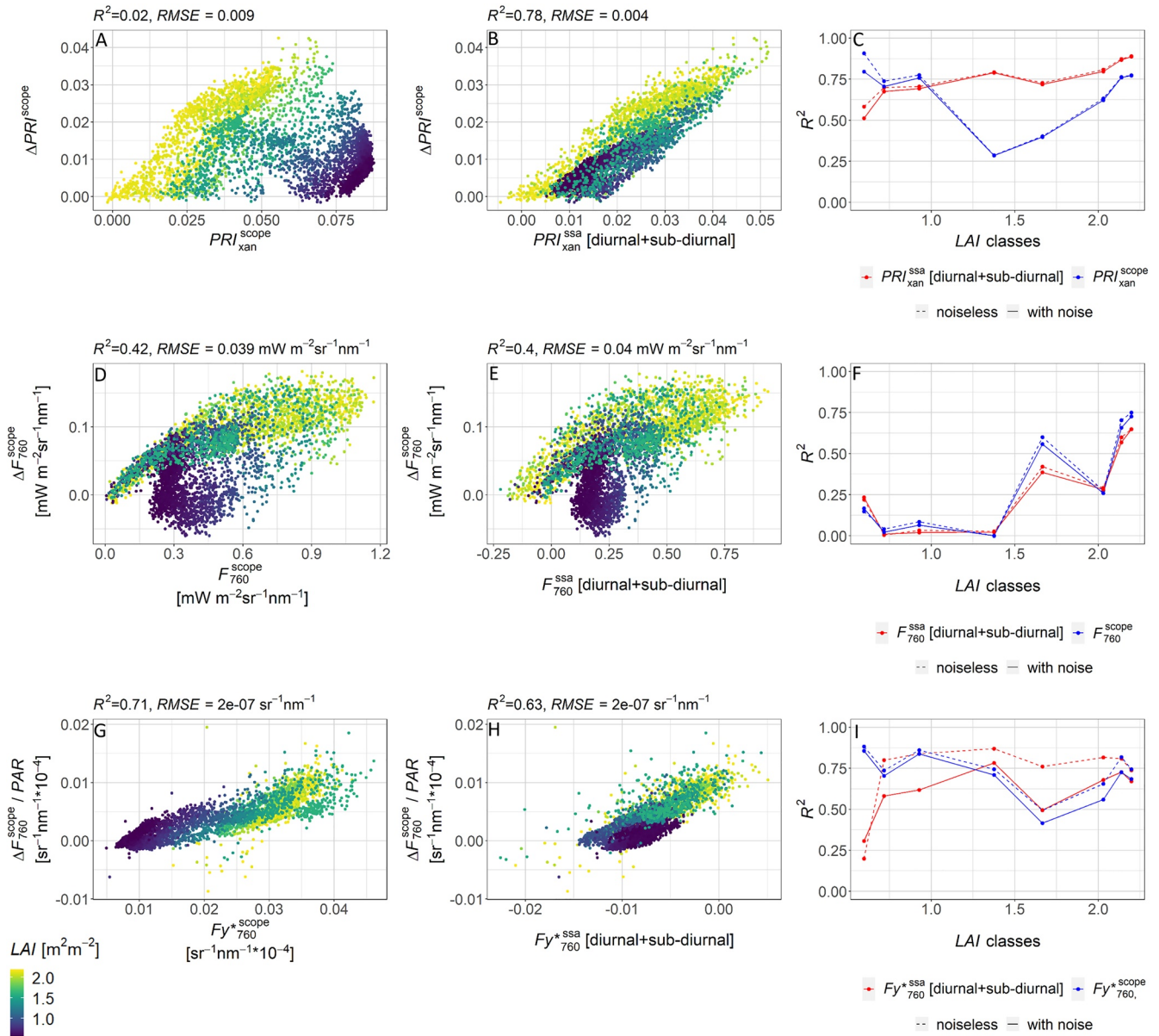


Figure 7. First row: (a) relationship between PRI_{xan}^{scope} and ΔPRI_{xan}^{scope} ; (b) relationship between PRI_{xan}^{ssa} (diurnal + sub-diurnal) and ΔPRI_{xan}^{scope} ; (c) R^2 for linear relationships (a) and (b) aggregated by leaf area index (LAI) classes of equal size excluding and including noise. Second row: (d) relationship between F_{760}^{scope} and ΔF_{760}^{scope} ; (e) relationship between F_{760}^{ssa} (diurnal + sub-diurnal) and ΔF_{760}^{scope} ; (f) R^2 for linear relationships (d) and (e) aggregated by LAI classes of equal size excluding and including noise. Third row: (g) relationship between $F_{y^*}^{scope}$ and $\Delta F_{760}^{scope} / PAR$; (h) relationship between $F_{y^*}^{ssa}$ (diurnal + sub-diurnal) and $\Delta F_{760}^{scope} / PAR$; (i) R^2 for linear relationships (g) and (h) aggregated by LAI classes of equal size excluding and including noise. The data presented in the figure correspond to daytime, $SZA \leq 80^\circ$ and the fraction of the day between 0.2 and 0.8.

are linked to the physiological response of vegetation (Figure 10). Based on the results from the modeling analyses (Figures 7–9), we filtered out data acquired in summer with $NDVI < 0.4$ (and, therefore, low LAI) (Figures 10a, 10b, 10d, 10e, 10g and 10h) and $R_{in} < 250 \text{ W m}^{-2}$ (Figures 10c, 10f and 10i).

PRI_m showed a weak correlation with LUE_m^{ssa} (diurnal+sub-diurnal) ($R^2 = 0.19$, Figure 10a). Fast SSA-decomposed PRI_m^{ssa} (diurnal+sub-diurnal) only slightly improved the correlation with LUE_m^{ssa} (diurnal+sub-diurnal) ($R^2 = 0.21$, Figure 10d) and showed higher R^2 for all $NDVI$ bins except a range of 0.6–0.67 (Figure 10g).

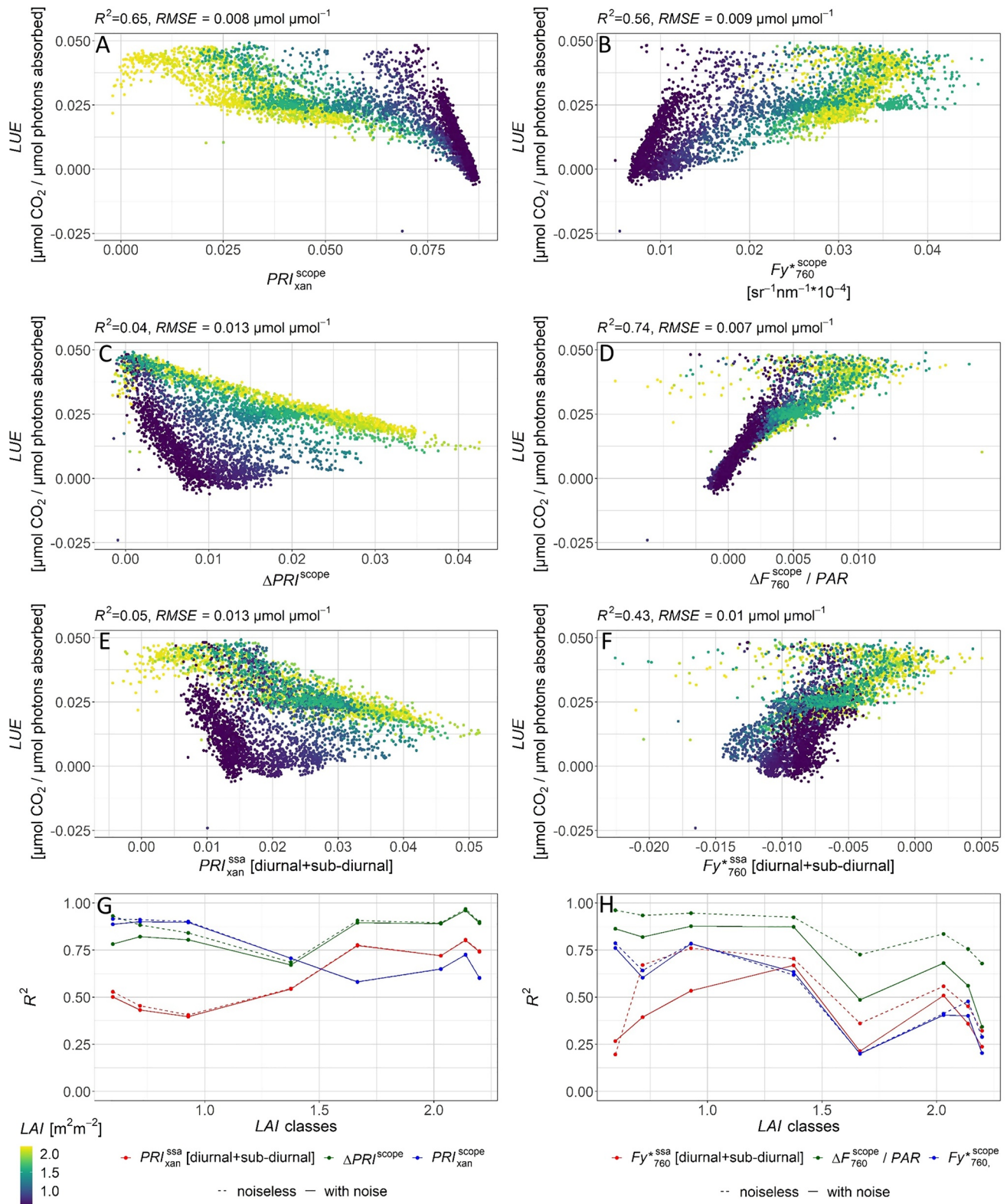


Figure 8.

Relationship between $F_{760,m}^{SSA}$ and LUE_m^{*SSA} (diurnal+sub-diurnal) showed considerably lower correlation ($R^2 = 0.08$, Figure 10e) compared to the relationship between original $F_{760,m}$ and LUE_m^{*SSA} (diurnal+sub-diurnal) ($R^2 = 0.17$, Figure 10b).

Out of three tested variables only the relationship between $Fy_{760,m}^{*SSA}$ (diurnal+sub-diurnal) and LUE_m^{*SSA} (diurnal+sub-diurnal) showed a significantly improved correlation compared to the relationship between undecomposed $Fy_{760,m}^*$ and LUE_m^{*SSA} (diurnal+sub-diurnal) ($R^2 = 0.42$ vs. $R^2 = 0.01$, Figures 10c and 10f). For all analyzed *NDVI* bins, the R^2 of $Fy_{760,m}^{*SSA}$ (diurnal+sub-diurnal) versus LUE_m^{*SSA} (diurnal+sub-diurnal) relationship was considerably higher (Figure 10i).

4. Discussion

4.1. Performance of SSA in Separating Seasonal and Fast Dynamics of *F* and *PRI*

With the increasing availability of high temporal resolution optical data collected simultaneously with CO_2 fluxes at EC stations (Balzarolo et al., 2011; Gamon, et al., 2006), it is pivotal to interpret the information provided by these data sets adequately. *PRI* and *F* are related to photosynthetic activity but confounded by biophysical parameters which vary at different timescales (Gamon & Berry, 2012). To our knowledge, there were no previous attempts to use time series decomposition as a tool to disentangle physiological information from these signals.

Our approach shows that SSA decomposition of PRI_{xan}^{scope} , F_{760}^{scope} , and Fy_{760}^{*scope} simulated with SCOPE for a specific case study of Mediterranean grassland ecosystem allowed to separate slow and fast varying components with different levels of accuracy. Following the two-components concept of *PRI* variability - constitutive and facultative, introduced in Gamon and Berry (2012), we showed that these components could be successfully distinguished using the highly data-adaptive SSA technique. The decomposed slow variability of the total PRI_{xan}^{scope} showed a high correlation with constitutive PRI_0^{scope} (Figure 6a), which is highly correlated with modified red-edge normalized difference index (*mNDI*), sensitive to chlorophyll content ($R^2 = 0.94$) (Sims & Gamon, 2002). This result is similar to the strong relationships emerging between *PRI* of perfectly dark-adapted leaves and *mNDI* obtained in Hmimina et al. (2014, 2015) and Merlier et al. (2015) at both leaf and canopy scales. The facultative variability ΔPRI_{xan}^{scope} was well predicted by the fast component PRI_{xan}^{SSA} extracted with SSA and varying at diurnal and sub-diurnal timescales (Figure 7a).

The potential to capture fast dynamics of spectral signals related to vegetation physiology was assessed by relating PRI_{xan}^{SSA} (diurnal + sub-diurnal) to *LUE*. The overall high R^2 (Figure 7c) gradually increased from low to high *LAI* values. In the modeled data set, the summer season combined low *LAI* and reduced water availability with highly variable *VPD* (daily range of 0–75 hPa) (Figure 3b) and *NPQ* values (daily range of 0–2.6). Under these severe conditions, there is a lack of *PRI* response to increasing *PAR*, which might explain the low correlation between PRI_{xan}^{SSA} (diurnal + sub-diurnal) and *LUE* found at this period of the year. The analyses of noiseless data discarded that these weak correlations in these circumstances were induced by noise (Figure 7c).

As shown in Figure 8a, total PRI_{xan}^{SSA} and *LUE* exhibit a non-linear relationship with variability in intercepts between *LAI* classes. The fast component of PRI_{xan}^{SSA} (diurnal + sub-diurnal), in turn, linearly correlated with *LUE* when the relationships were considered for the periods of similar *LAI* (Figures 8g and 9g). Previous works of Hmimina et al. (2014, 2015), evaluated the relationships of total and pigment-corrected *PRI* with *LUE* for short periods, excluding sources of significant *LAI* changes. We assessed the SSA decomposition

Figure 8. First column: (a) relationship between PRI_{xan}^{scope} and light-use efficiency (*LUE*); (c) relationship between ΔPRI_{xan}^{scope} and *LUE*; (e) relationship between PRI_{xan}^{SSA} (diurnal+sub-diurnal) and *LUE*; (g) R^2 for linear relationships (a), (c), (e) aggregated by *LAI* classes of equal size excluding and including noise. Second column: (b) relationship between Fy_{760}^{*scope} and *LUE*; (d) relationship between $\Delta F_{760}^{scope} / PAR$ and *LUE*; (f) relationship between Fy_{760}^{*SSA} (diurnal+sub-diurnal) and *LUE*; (h) R^2 for linear relationships (b), (d), (f) aggregated by *LAI* classes of equal size excluding and including noise. The data presented in the figure correspond to daytime, $SZA \leq 80^\circ$ and the fraction of the day between 0.2 and 0.8.

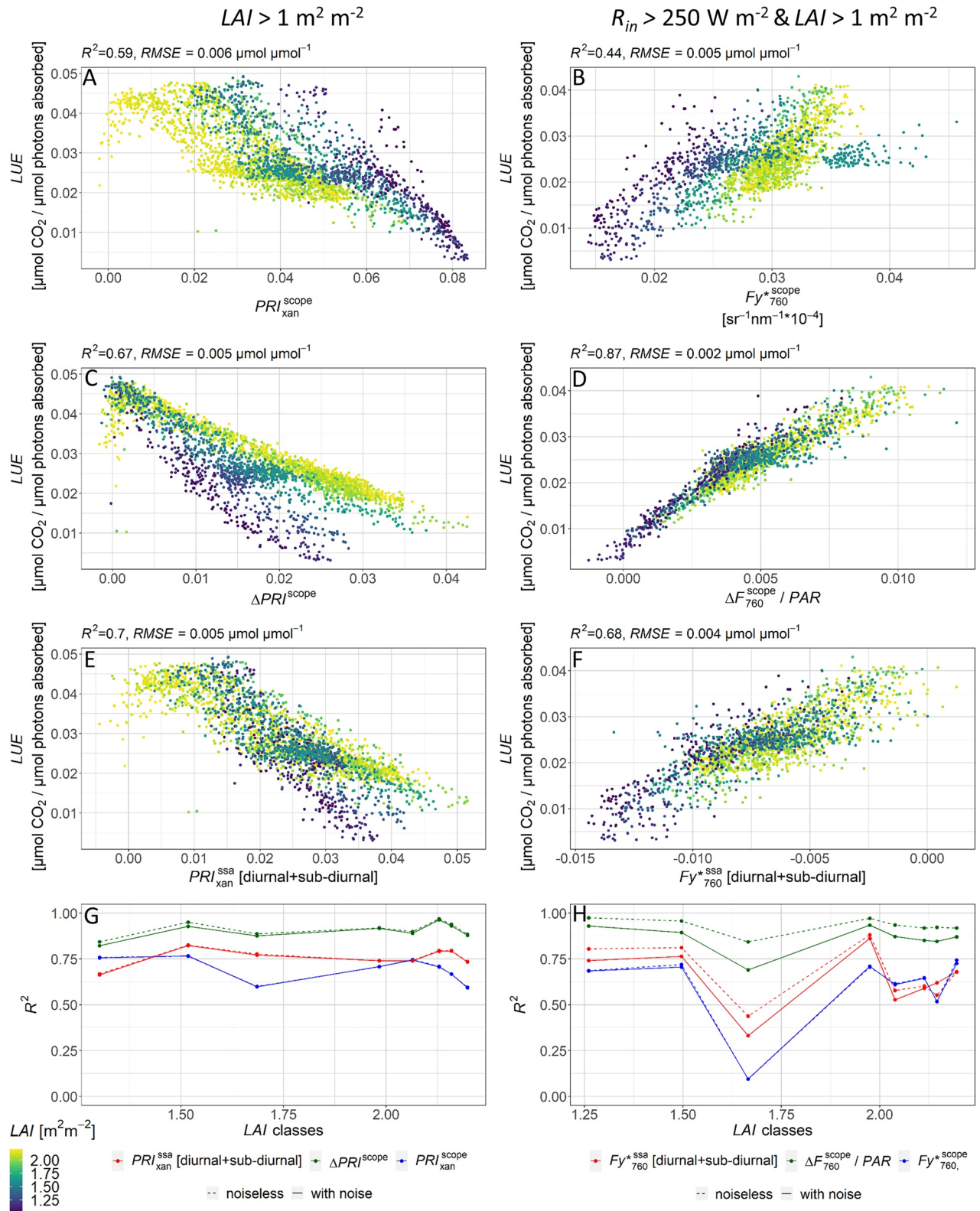


Figure 9.

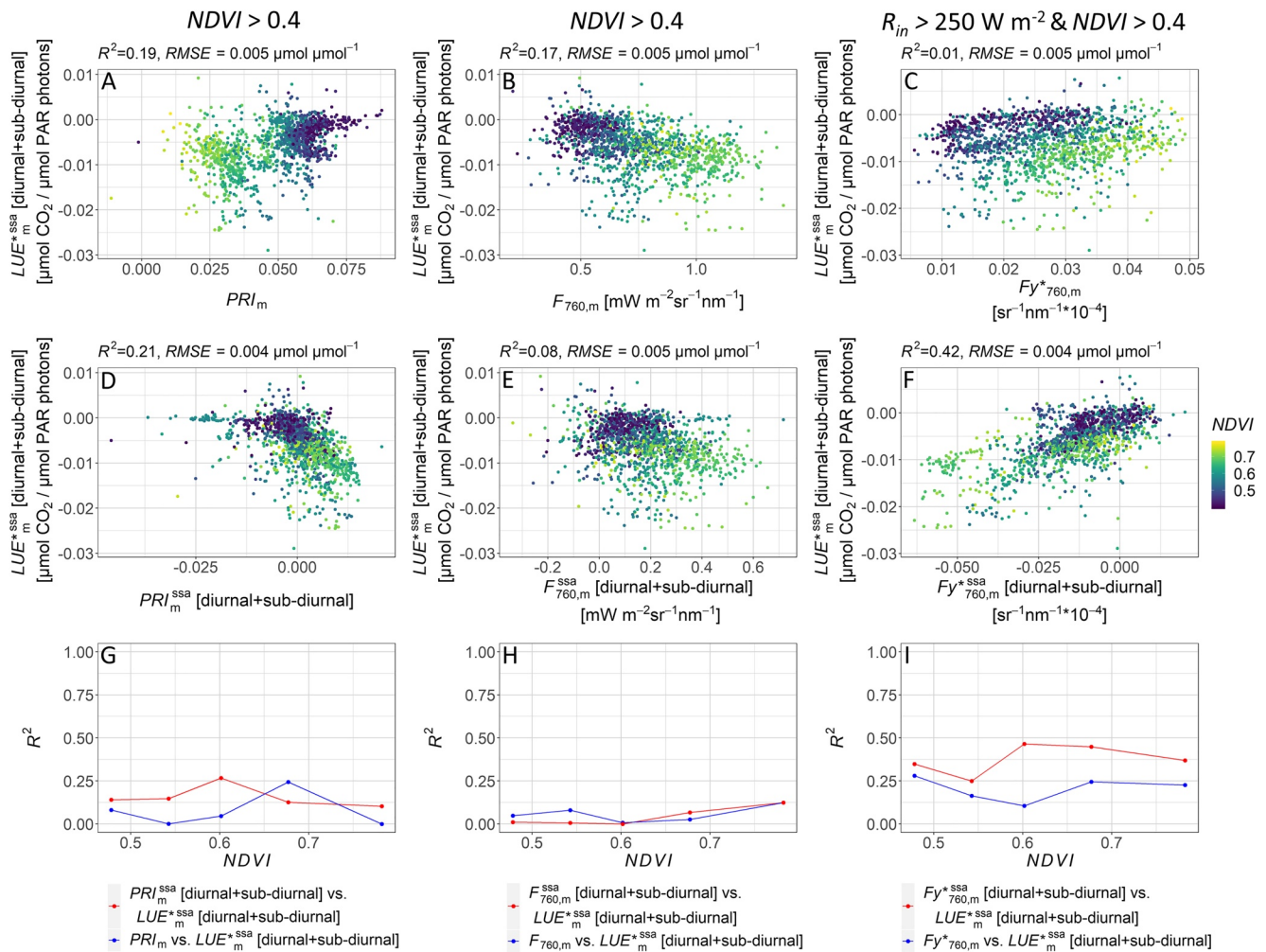


Figure 10. First column: (a) relationships between PRI_m and LUE_m^{*ssa} (diurnal+sub-diurnal); (d) PRI_m^{ssa} (diurnal+sub-diurnal) and LUE_m^{*ssa} (diurnal+sub-diurnal); (g) R^2 for linear relationships (a), (d) aggregated by NDVI classes of equal size excluding and including noise. Second column: (b) relationships between $F_{760,m}$ and LUE_m^{*ssa} (diurnal+sub-diurnal); (e) $F_{760,m}^{ssa}$ (diurnal+sub-diurnal) and LUE_m^{*ssa} (diurnal+sub-diurnal); (h) R^2 for linear relationships (b), (e) aggregated by NDVI classes of equal size excluding and including noise. Third column: (c) relationships between $Fy_{760,m}^{*ssa}$ and LUE_m^{*ssa} (diurnal + sub-diurnal); (f) $Fy_{760,m}^{*ssa}$ (diurnal + sub-diurnal) and LUE_m^{*ssa} (diurnal + sub-diurnal); (i) R^2 for linear relationships (c), (f) aggregated by NDVI classes of equal size excluding and including noise. The data presented in the figure correspond to daytime data, $SZA \leq 80^\circ$, $NDVI > 0.4$ (a, b, d, e, g, and h), and $R_{in} < 250 \text{ W m}^{-2}$ (c, f, and i).

under varying LAI and found a strong sensitivity of the models to this parameter which should not be disregarded.

Despite the robustness to noise and the capability of SSA to capture the facultative component of PRI (Figures 7a–7c), the relationship between measured LUE_m^{*ssa} (diurnal + sub-diurnal) and PRI_m^{ssa} (diurnal + sub-diurnal) was not significantly improved compared to the relationship between LUE_m (diurnal + sub-diurnal) and original PRI_m (Figures 10a and 10d). This might be explained by the fact that under the strong seasonal variability of the Mediterranean ecosystem (in terms of pigment pool and LAI), the PRI signal itself covaries with LUE in a way that, after all the uncertainties, SSA decomposition cannot offer

Figure 9. First column, leaf area index (LAI) $> 1 \text{ m}^2 \text{ m}^{-2}$: (a) relationship between PRI_{xan}^{scope} and light-use efficiency (LUE); (c) relationship between ΔPRI_{xan}^{scope} and LUE ; (e) relationship between PRI_{xan}^{ssa} (diurnal+sub-diurnal) and LUE ; (g) R^2 for linear relationships (a), (c), (e) aggregated by LAI classes of equal size excluding and including noise. Second column, LAI $> 1 \text{ m}^2 \text{ m}^{-2}$ and $R_{in} < 250 \text{ W m}^{-2}$: (b) relationship between Fy_{760}^{scope} and LUE ; (d) relationship between $\Delta F_{760}^{scope} / PAR$ and LUE ; (f) relationship between Fy_{760}^{*ssa} (diurnal+sub-diurnal) and LUE ; (h) R^2 for linear relationships (b), (d), (f) aggregated by LAI classes of equal size excluding and including noise. The data presented in the figure correspond to daytime, $SZA \leq 80^\circ$ and the fraction of the day between 0.2 and 0.8.

significant advantage respect to the original signal. However, this could be a valuable tool in less dynamic ecosystems, such as evergreen forests, where the estimation of ΔPRI has provided additional access to LUE (Hilker et al., 2008). Also, it must be considered that PRI_m^{ssa} (diurnal + sub-diurnal) may capture additional sources of variation. On the one hand, PRI_{xan}^{ssa} (diurnal + sub-diurnal) responds to diurnal and sub-diurnal variations of NPQ driven by instantaneous changes in light intensity (Krause & Weis, 1991) and modulated by VPD and T_{air} (Demmig-Adams & Adams, 1992); on the other hand, these are mixed with directional effects (i.e., sun position and illumination conditions) imposed on diurnal cycles of PRI (Biriukova et al., 2020; Hall et al., 2008; Hilker et al., 2008). Both processes vary in the same frequency bin and only change in amplitude, and SSA might be unable to separate these two components.

The capability of SSA to decouple slow and fast dynamics in the fluorescence signal was evaluated for both modeled F_{760}^{scope} and Fy_{760}^{*scope} and measured $F_{760,m}$ and $Fy_{760,m}^*$. First, we attempted to disentangle $aPAR$ -related and physiology-related variabilities in F_{760}^{scope} . F variability driven only by biophysical vegetation properties and irradiance ($F_{0,760}^{scope}$) was not accurately captured with F_{760}^{ssa} (seasonal) ($R^2 = 0.46$) (Figure 6b). Also, fast physiological changes (ΔF_{760}^{scope}) were not better predicted by F_{760}^{ssa} (diurnal + sub-diurnal) compared to the original undecomposed F_{760}^{scope} (Figures 7e and 7f). The problem with the SSA decomposition of F_{760}^{scope} can be explained by the fact that both $F(F_{760}^{scope})$ and $F_{0,760}^{scope}$ are strongly driven by $aPAR$ and highly correlated with each other ($R^2 = 0.98$). Therefore, the contribution of $aPAR$ -related variability and physiology-related component is hard for SSA to decouple since both show a substantial variability at the same temporal scale. By normalizing F_{760}^{scope} with PAR we removed the part of the variability attributed to irradiance and reduced the number of unknowns in the LUE model (Equation 2).

We hypothesized that by decomposing Fy_{760}^{*scope} , we can remove a part of the variability attributed to $faPAR_{Cab}$ and infer information related to fluorescence efficiency ϕ'_f . Seasonal variability, associated with $faPAR_{Cab}$ (R^2 of the relationship between $Fy_{0,760}^{*scope}$ and $faPAR_{Cab}$ is 0.99) was captured by the SSA-reconstructed Fy_{760}^{*ssa} (seasonal) (Figure 6c). The remaining variability attributed to physiological modulation of ΔF_{760}^{scope} normalized by PAR was better predicted by Fy_{760}^{*ssa} (diurnal + sub-diurnal) than by Fy_{760}^{*scope} (Figure 7i) above a certain LAI threshold. The decomposition of Fy_{760}^{*scope} was more sensitive to noise than the decomposition of PRI ; however, in all the cases, the method resulted inaccurate at low LAI . This might imply the existence of a minimum ΔF_{760}^{scope} threshold for SSA to capture its fast variability. Discarding data modeled with $LAI < 1 \text{ m}^2 \text{ m}^{-2}$ improved the estimation of $\Delta F_{760}^{scope} / PAR$ with Fy_{760}^{*ssa} (diurnal + sub-diurnal) (Figure S3). Despite the sensitivity to noise, when limited to a sufficient LAI range, SSA successfully decoupled physiology-related information from apparent fluorescence yield both in the modeled data set Fy_{760}^{*ssa} (diurnal + sub-diurnal) versus LUE (Figures 8f, 8h, 9f and 9h) and in the measured data set $Fy_{760,m}^{*ssa}$ (diurnal + sub-diurnal) versus LUE_m^{*ssa} (diurnal+sub-diurnal) (Figures 10f and 10i). The evaluation of this tool on simulated data provided a valuable insight into the limitations and strengths of SSA in terms of noise and variable space, both for the estimation of physiologically driven fast variability and the relationship of these estimates to variables of physiological interest (LUE).

The choice of SSA decomposition parameters plays an important role in the reconstruction of time series. The decomposition can be potentially improved by varying the “cut-offs” of the frequency bins (Table S1) in which we aim to extract the subsignals. Here we tested different frequency bins of varying length and borders and heuristically chose broader bins covering three timescales interesting from an ecological point of view — seasonal, diurnal, and sub-diurnal. Depending on the time series length and temporal resolution, the borders of the frequency bins of interest might be expanded (e.g., if sampling frequency is lower, there is no need to detect sub-diurnal components), or narrowed (e.g., in case of sampling frequency higher than 30 min would be interesting to have several bins per day to explore the dynamics of the fast physiological response at different timescales during a day).

4.2. Limitations and Applicability to Field Data

This study is a model-based proof of concept for decoupling slow dynamics related to biochemical composition and structural changes and fast physiological dynamics in TOC time series of F and PRI . We chose a

model-based study because the variables required to evaluate the proposed decomposition technique (i.e., a combination of canopy scale passive and leaf-level active measurements) are only sparsely available and prone to uncertainty related to the scaling from leaf- to canopy-level processes such as *NPQ*. In this context, the use of synthetic data generated by a state-of-the-art process-based model allowed evaluating whether SSA can disentangle the processes acting at different timescales as encoded in the model. This kind of model-based evaluation has been successfully used for various problems lacking suitable data sets (e.g., Nelson et al., 2018). However, it should be noted that SCOPE is not a dynamic model. This implies that the model does not capture some of the physiological responses (i.e., sustained *NPQ*) that can be observed in the field. When analyzing the links between decomposed *PRI* and *NPQ*, it should be considered that *NPQ* involves mechanisms operating at different temporal scales, such as reversible energy-dependent *NPQ* with overnight relaxation and sustained *NPQ* operating at longer timescales (Porcar-Castell, 2011). However, predicting *NPQ* based on *PRI* is only possible when reversible *NPQ* is dominating and sustained *NPQ* is insignificant (Alonso et al., 2017). In SCOPE simulations, we kept a constant rate of sustained *NPQ*, so that modeled *NPQ* only includes the effect of the xanthophyll cycle activation. Therefore, when applying SSA to field data, one should consider that decomposed fast components of *PRI* may not represent the total variability of *NPQ*.

Additional considerations are associated with the parameterization of SCOPE fluorescence module with data sets limited to few species (i.e., cotton), which may also affect the accuracy of the representation of the physiological response of grassland ecosystem. Nevertheless, we assume that for the purpose of the decomposition of slow and fast temporal dynamics of *F* and *PRI* with SSA SCOPE provided reasonable variabilities controlled by physiological and non-physiological vegetation properties.

Another limitation of the method arises in the case of structurally complex canopies. SCOPE model relies on the approach of SAIL, which represents a homogeneous canopy of randomly distributed leaves. This approach cannot reliably represent canopies with a strong geometrical component due to a heterogeneous 3D structure. *PRI* and fluorescence models have been implemented in 3D RTMs such as FluorFLIGHT (Hernández-Clemente et al., 2017) or DART (Gastellu-Etchegorry et al., 2017); however, these implementations mainly limit to the radiative transfer of these signals, and lack of a coherent coupling with photosynthetic efficiency at a comparable level of detail. Further research is needed in the case of structurally complex canopies, but current models do not yet allow such detailed analyses.

SSA decomposition requires high temporal resolution data, acquired with at least 1 h–30 min interval to track the fast physiological response of *F* and activation of the xanthophyll cycle, occurring at timescales of minutes after changes in light intensity (Müller et al., 2001). In general, the higher the temporal resolution of the time series, the more accurate extraction of fast varying physiological components can be achieved. With the expanding network of automated proximal sensing systems (Aasen et al., 2019; Cogliati et al., 2015), continuous and high-resolution time series of *F* and *R* (as measured in Majadas de Tiétar, Figure 10) become increasingly available.

These systems can be used to acquire time series of *PAR*, *PRI*, and *F*, as well as normalized vegetation indices informing on vegetation structure. Often, these systems are installed close to EC sites, which provide measurements of *NEE*, partitioned on *GPP* and respiration, and auxiliary abiotic variables (Rebmann et al., 2018), which would be helpful for the evaluation of SSA decomposition performance under different environmental conditions. Some EC sites also provide measurements of *aPAR*, but often this term has to be modeled from remote sensing observations, which is still challenging. Apparent *LUE** (*GPP/PAR*) and fluorescence yield F_y^* (*F/PAR*) are usually easier to obtain in comparison to metrics derived using *aPAR* or *aPAR*_{cab}. Gitelson and Gamon (2015) showed that *LUE* computed as *GPP/PAR* is the *LUE* estimate the most confounded by canopy structure among other *LUE* formulations. Contrarily, *LUE* computed as *GPP/aPAR*_{cab} mostly depends on the physiological status of vegetation. *aPAR* can be estimated using several downward and upward-facing quantum sensors installed above and below the canopy (Inoue et al., 2008; Jenkins et al., 2007) or using automated observation systems based on LED sensors (Kim et al., 2019). *aPAR*_{cab} can be effectively retrieved from field spectral reflectance and transmittance measurements (Serrano et al., 2000) or approximated using vegetation greenness indices (e.g., *NDVI*). However, there is still no standard procedure to accurately estimate *aPAR*_{cab} from optical reflectance factors. In this study, we showed the applicability of the SSA decomposition on commonly available F_{y760}^* and evaluated its relationship with

LUE computed as $GPP/aPAR_{Cab}$ and with SSA-decomposed fast component of LUE_m^{*ssa} (diurnal + sub-diurnal) to assess whether the fast component of Fy_{760}^* is related to physiological status of vegetation.

In addition to time series of optical variables, leaf-level pulse amplitude-modulated (PAM) measurements of NPQ , ϕ_f , and ϕ_p would be greatly beneficial for validating the decomposition results. For example, simultaneous installation of automated high spectral resolution devices (e.g., FloX system, JB Hyperspectral Devices UG, Germany) with micro-PAM (Atherton et al., 2016; Magney et al., 2017; Porcar-Castell et al., 2008) can provide a data set for the validation of the method. However, the availability of these coupled datasets is still very limited.

Since SSA requires data continuity, gap-filling should be applied to time series with missing values. For this purpose, SSA has also been successfully used as a gap-filling tool (Buttler et al., 2014; Mahecha et al., 2007). The classical SSA algorithm was modified so that SSA components are estimated based on non-missing values only, and the values of the reconstructions are imputed to missing values (Golyandina & Osipov, 2007). For night-time data, a noisy baseline should be provided as well, for example, by linearly interpolating the last daytime observation of a day and the first daytime observation of the following day, or by applying a moving window to smooth a baseline. One of the reasons why SSA-decomposition of measured data presented here did not yield robust results in the case of PRI_m (Figures 10a, 10d and 10g) might be long gaps in the time series (up to two months of missing data). In the future, the method should be tested on longer and more continuous time series.

Acknowledgments

This study has received funding from the European Union's Horizon 2020 research and innovation program under the Marie Skłodowska-Curie grant agreement No 721995. J. Pacheco-Labrador, M. Migliavacca acknowledge the DLR project OBEF-Accross2 "The Potential of Earth Observations to Capture Patterns of Biodiversity" (Contract No. 50EE1912, German Aerospace Center). The authors acknowledge the project SynerTGE "Landsat-8+Sentinel-2: exploring sensor synergies for monitoring and modeling key vegetation biophysical variables in tree-grass ecosystems" (CGL2015-69095-R, MINECO/FEDER, UE); and the project FLUXPEC "Monitoring changes in water and carbon fluxes from remote and proximal sensing in Mediterranean "dehesa" ecosystem" (CGL2012-34383, Spanish Ministry of Economy and Competitiveness). K. Biriukova thanks Anton Evdokimov and Marco Celesti for their help with data analysis. The authors thank the technical assistance provided by MPI-BGC Freiland Group, especially Olaf Kolle, Martin Hertel as well as Arnaud Carrara and Ramón López-Jiménez (CEAM); as well as the support of colleagues from MPI-BGC, especially Tarek El-Madany and David Martini, University of Extremadura, University of Milano-Bicocca, Speclab-CSIC, INIA, and CEAM involved in numerous field and laboratory works. The authors also appreciate the valuable comments and suggestions from Xi Yang, MaPi Cendrero-Mateo, and the two anonymous reviewers who helped improve this study. Open access funding enabled and organized by Projekt DEAL.

5. Conclusions

Automated proximal sensing is a powerful complement of gas exchange measurements in ecosystem stations monitoring water and carbon fluxes. It provides spectral signals (F and PRI) encompassing information on light-use in the photosynthetic machinery. Therefore, proximal sensing can improve our understanding of ecosystem function variability in time. However, these signals are affected by additional confounding factors operating at different temporal scales. We demonstrated the capability of SSA to separate the components related to canopy structural/biochemical properties and physiology of these signals from a simulated realistic time series of spectral and physiological variables. This decomposition was especially successful in the case of PRI and Fy_{760}^* , whose relationship with light-use efficiency was strong but still dependent on LAI . Application of the method on measured data showed promising results in the case of Fy_{760}^* . We expect that applying SSA to automated continuous measurements will improve the contribution of proximal sensing to the characterization of ecosystem functional properties.

Conflict of Interest

The authors declare no conflicts of interest relevant to this study.

Data Availability Statement

Datasets for this research are available in these intext data citation references: Biriukova et al. (2021).

References

- Aasen, H., Van Wittenberghe, S., Medina, N. S., Damm, A., Goulas, Y., Wieneke, S., et al. (2019). Sun-induced chlorophyll fluorescence II: Review of passive measurement setups, protocols, and their application at the leaf to canopy level. *Remote Sensing*, 11(8), 1–32. <https://doi.org/10.3390/rs11080956>
- Alonso, L., Van Wittenberghe, S., Amorós-López, J., Vila-Francés, J., Gómez-Chova, L., & Moreno, J. (2017). Diurnal cycle relationships between passive fluorescence, PRI and NPQ of vegetation in a controlled stress experiment. *Remote Sensing*, 9(8), 770. <https://doi.org/10.3390/rs9080770>
- Atherton, J., Nichol, C. J., & Porcar-Castell, A. (2016). Using spectral chlorophyll fluorescence and the photochemical reflectance index to predict physiological dynamics. *Remote Sensing of Environment*, 176, 17–30. <https://doi.org/10.1016/j.rse.2015.12.036>
- Baldocchi, D., Valentini, R., Running, S., Oechel, W., & Dahlman, R. (1996). Strategies for measuring and modelling carbon dioxide and water vapour fluxes over terrestrial ecosystems. *Global Change Biology*, 2(3). <https://doi.org/10.1111/j.1365-2486.1996.tb00069.x>
- Balzarolo, M., Anderson, K., Nichol, C., Rossini, M., Vescovo, L., Arriga, N., et al. (2011). Ground-based optical measurements at European flux sites: A review of methods, instruments and current controversies. *Sensors*, 11(8), 7954–7981. <https://doi.org/10.3390/s110807954>

- Biriukova, K., Celesti, M., Evdokimov, A., Pacheco-Labrador, J., Julitta, T., Migliavacca, M., et al. (2020). Effects of varying solar-view geometry and canopy structure on solar-induced chlorophyll fluorescence and PRI. *International Journal of Applied Earth Observation and Geoinformation*, 89, 102069. <https://doi.org/10.1016/j.jag.2020.102069>
- Biriukova, K., Pacheco-Labrador, J., Migliavacca, M., Mahecha, M., Gonzalez-Cascon, R., Pilar Martin, M., & Rossini, M. (2021). Time series of fluxes, biochemical and spectral variables simulated with SCOPE model and acquired in a Mediterranean grassland for SSA. *Figshare Dataset*. <https://doi.org/10.6084/m9.figshare.13190858>
- Broomhead, D. S., & King, G. P. (1986). Extracting qualitative dynamics from experimental data. *Physica D: Nonlinear Phenomena*, 20(2–3), 217–236. [https://doi.org/10.1016/0167-2789\(86\)90031-X](https://doi.org/10.1016/0167-2789(86)90031-X)
- Buttlar, J. V. (2015). *Package 'spectral.methods'*, 29.
- Buttlar, J. V., Zscheischler, J., & Mahecha, M. D. (2014). An extended approach for spatiotemporal gapfilling: Dealing with large and systematic gaps in geoscientific datasets. *Nonlinear Processes in Geophysics*, 21(1), 203–215. <https://doi.org/10.5194/npg-21-203-2014>
- Cogliati, S., Rossini, M., Julitta, T., Meroni, M., Schickling, A., Burkart, A., et al. (2015). Continuous and long-term measurements of reflectance and sun-induced chlorophyll fluorescence by using novel automated field spectroscopy systems. *Remote Sensing of Environment*, 164, 270–281. <https://doi.org/10.1016/j.rse.2015.03.027>
- Collatz, G. J., Ball, J. T., Grivet, C., & Berry, J. A. (1991). Physiological and environmental regulation of stomatal conductance, photosynthesis and transpiration: A model that includes a laminar boundary layer. *Agricultural and Forest Meteorology*, 54(2–4), 107–136. [https://doi.org/10.1016/0168-1923\(91\)90002-8](https://doi.org/10.1016/0168-1923(91)90002-8)
- Demmig-Adams, B. (1990). Carotenoids and photoprotection in plants: A role for the xanthophyll zeaxanthin. In *BBA-Bioenergetics*, 1020(1), 1–24. [https://doi.org/10.1016/0005-2728\(90\)90088-L](https://doi.org/10.1016/0005-2728(90)90088-L)
- Demmig-Adams, B., & Adams, W. W. (1992). Photoprotection and other responses of plants to high light stress. *Annual Review of Plant Physiology and Plant Molecular Biology*, 43(1), 599–626. <https://doi.org/10.1146/annurev.pp.43.060192.003123>
- Demmig-Adams, B., & Adams, W. W. (1996). The role of xanthophyll cycle carotenoids in the protection of photosynthesis. *Trends in Plant Science*, 1(1), 21–26. [https://doi.org/10.1016/S1360-1385\(96\)80019-7](https://doi.org/10.1016/S1360-1385(96)80019-7)
- El-Madany, T. S., Reichstein, M., Perez-Priego, O., Carrara, A., Moreno, G., Pilar Martín, M., et al. (2018). Drivers of spatio-temporal variability of carbon dioxide and energy fluxes in a Mediterranean savanna ecosystem. *Agricultural and Forest Meteorology*, 262, 258–278. <https://doi.org/10.1016/j.agrformet.2018.07.010>
- Filella, I., Porcar-Castell, A., Munné-Bosch, S., Bäck, J., Garbulska, M. F., & Peñuelas, J. (2009). PRI assessment of long-term changes in carotenoids/chlorophyll ratio and short-term changes in de-epoxidation state of the xanthophyll cycle. *International Journal of Remote Sensing*, 30(17), 4443–4455. <https://doi.org/10.1080/01431160802575661>
- Fraedrich, K. (1986). Estimating the dimensions of weather and climate attractors. *Journal of the Atmospheric Sciences*, 43(5), 419–432. [https://doi.org/10.1175/1520-0469\(1986\)043<0419:etdowa>2.0.co;2](https://doi.org/10.1175/1520-0469(1986)043<0419:etdowa>2.0.co;2)
- Frankenberg, C., & Berry, J. (2018). Solar induced chlorophyll fluorescence: Origins, relation to photosynthesis and retrieval. In *Comprehensive remote sensing* (Issue 1986). Elsevier. <https://doi.org/10.1016/b978-0-12-409548-9.10632-3>
- Gamon, J. A., & Berry, J. A. (2012). Facultative and constitutive pigment effects on the photochemical reflectance index (PRI) in sun and shade conifer needles. *Israel Journal of Plant Sciences*, 60(1–2), 85–95. <https://doi.org/10.1560/IJPS.60.1-2.85>
- Gamon, J. A., Peñuelas, J., & Field, C. B. (1992). A narrow-waveband spectral index that tracks diurnal changes in photosynthetic efficiency. *Remote Sensing of Environment*, 41(1), 35–44. [https://doi.org/10.1016/0034-4257\(92\)90059-S](https://doi.org/10.1016/0034-4257(92)90059-S)
- Gamon, J. A., Rahman, A. F., Dungan, J. L., Schildhauer, M., & Huemmrich, K. F. (2006). Spectral network (SpecNet)-What is it and why do we need it? *Remote Sensing of Environment*, 103(3), 227–235. <https://doi.org/10.1016/j.rse.2006.04.003>
- Garbulska, M. F., Peñuelas, J., Gamon, J., Inoue, Y., & Filella, I. (2011). The photochemical reflectance index (PRI) and the remote sensing of leaf, canopy and ecosystem radiation use efficiencies. A review and meta-analysis. *Remote Sensing of Environment*, 115(2), 281–297. <https://doi.org/10.1016/j.rse.2010.08.023>
- Gastellu-Etchegorry, J. P., Lauret, N., Yin, T., Landier, L., Kallel, A., Malenovsky, Z., et al. (2017). DART: Recent advances in remote sensing data modeling with atmosphere, polarization, and chlorophyll fluorescence. *IEEE Journal of Selected Topics in Applied Earth Observations and Remote Sensing*, 10(6), 2640–2649. <https://doi.org/10.1109/JSTARS.2017.2685528>
- Ghil, M., Allen, M. R., Dettinger, M. D., Ide, K., Kondrashov, D., Mann, M. E., et al. (2002). Advanced spectral methods for climatic time series. *Reviews of Geophysics*, 40(1), 1003. <https://doi.org/10.1029/2000RG000092>
- Gitelson, A. A., & Gamon, J. A. (2015). The need for a common basis for defining light-use efficiency: Implications for productivity estimation. *Remote Sensing of Environment*, 156, 196–201. <https://doi.org/10.1016/j.rse.2014.09.017>
- Golyandina, N., & Korobeynikov, A. (2014). Basic singular spectrum analysis and forecasting with R. *Computational Statistics and Data Analysis*, 71, 934–954. <https://doi.org/10.1016/j.csda.2013.04.009>
- Golyandina, N., Korobeynikov, A., & Zhigljavsky, A. (2018). Singular spectrum analysis with R. In *Singular Spectrum analysis*. Springer Berlin Heidelberg. <https://doi.org/10.1007/978-3-662-57380-8>
- Golyandina, N., Nekrutkin, V., & Zhigljavsky, A. (2001). Analysis of time series structure: SSA and related techniques. In CHAPMAN & HALL/CRC (Vol. 97, pp. 1207–1208). <https://doi.org/10.1198/jasa.2002.s239>
- Golyandina, N., & Osipov, E. (2007). The “Caterpillar”-SSA method for analysis of time series with missing values. *Journal of Statistical Planning and Inference*, 137(8), 2642–2653. <https://doi.org/10.1106/jjspi.2006.05.014>
- Golyandina, N., & Zhigljavsky, A. (2013). *Singular Spectrum analysis for time series*. <https://doi.org/10.1007/978-3-642-34913-3>
- Hall, F. G., Hilker, T., Coops, N. C., Lyapustin, A., Huemmrich, K. F., Middleton, E., et al. (2008). Multi-angle remote sensing of forest light use efficiency by observing PRI variation with canopy shadow fraction. *Remote Sensing of Environment*, 112(7), 3201–3211. <https://doi.org/10.1016/j.rse.2008.03.015>
- Hernández-Clemente, R., North, P. R. J., Hornero, A., & Zarco-Tejada, P. J. (2017). Assessing the effects of forest health on sun-induced chlorophyll fluorescence using the FluorFLIGHT 3-D radiative transfer model to account for forest structure. *Remote Sensing of Environment*, 193, 165–179. <https://doi.org/10.1016/j.rse.2017.02.012>
- Hilker, T., Coops, N. C., Hall, F. G., Black, T. A., Wulder, M. A., Nesic, Z., & Krishnan, P. (2008). Separating physiologically and directionally induced changes in PRI using BRDF models. *Remote Sensing of Environment*, 112(6), 2777–2788. <https://doi.org/10.1016/j.rse.2008.01.011>
- Hmimina, G., Duffrène, E., & Soudani, K. (2014). Relationship between photochemical reflectance index and leaf ecophysiological and biochemical parameters under two different water statuses: Towards a rapid and efficient correction method using real-time measurements. *Plant, Cell and Environment*, 37(2), 473–487. <https://doi.org/10.1111/pce.12171>

- Hmimina, G., Merlier, E., Dufrène, E., & Soudani, K. (2015). Deconvolution of pigment and physiologically related photochemical reflectance index variability at the canopy scale over an entire growing season. *Plant, Cell and Environment*, 38(8), 1578–1590. <https://doi.org/10.1111/pce.12509>
- Inoue, Y., Peñuelas, J., Miyata, A., & Mano, M. (2008). Normalized difference spectral indices for estimating photosynthetic efficiency and capacity at a canopy scale derived from hyperspectral and CO₂ flux measurements in rice. *Remote Sensing of Environment*, 112(1), 156–172. <https://doi.org/10.1016/j.rse.2007.04.011>
- Jenkins, J. P., Richardson, A. D., Braswell, B. H., Ollinger, S. V., Hollinger, D. Y., & Smith, M. L. (2007). Refining light-use efficiency calculations for a deciduous forest canopy using simultaneous tower-based carbon flux and radiometric measurements. *Agricultural and Forest Meteorology*, 143(1–2), 64–79. <https://doi.org/10.1016/j.agrformet.2006.11.008>
- Kim, J., Ryu, Y., Dechant, B., Lee, H., Kim, H. S., Kornfeld, A., & Berry, J. A. (2021). Solar-induced chlorophyll fluorescence is non-linearly related to canopy photosynthesis in a temperate evergreen needleleaf forest during the fall transition. *Remote Sensing of Environment*, 258, 112362. <https://doi.org/10.1016/j.rse.2021.112362>
- Kim, J., Ryu, Y., Jiang, C., & Hwang, Y. (2019). Continuous observation of vegetation canopy dynamics using an integrated low-cost, near-surface remote sensing system. *Agricultural and Forest Meteorology*, 264, 164–177. <https://doi.org/10.1016/j.agrformet.2018.09.014>
- Korobeynikov, A. A., Shlemov, A., Usevich, K., Golyandina, N., & Korobeynikov, M. A. (2017). *Title A collection of methods for singular spectrum analysis*. Retrieved from <http://github.com/asl/rssa>
- Krause, G. H., & Weis, E. (1991). Chlorophyll fluorescence and photosynthesis: The basics. *Annual Review of Plant Physiology and Plant Molecular Biology*, 42(1), 313–349. <https://doi.org/10.1146/annurev.pp.42.060191.001525>
- Lee, J. E., Frankenberg, C., van der Tol, C., Berry, J. A., Guanter, L., Boyce, C. K., et al. (2013). Forest productivity and water stress in Amazonia: Observations from GOSAT chlorophyll fluorescence. *Tohoku Journal of Experimental Medicine*, 230(1). <https://doi.org/10.1098/rspb.2013.0171>
- Luo, Y., El-Madany, T., Ma, X., Nair, R., Jung, M., Weber, U., et al. (2020). Nutrients and water availability constrain the seasonality of vegetation activity in a Mediterranean ecosystem. *Global Change Biology*, 26, 4379–4400. <https://doi.org/10.1111/gcb.15138>
- Luo, Y., El-Madany, T. S., Filippa, G., Ma, X., Ahrens, B., Carrara, A., et al. (2018). Using near-infrared-enabled digital repeat photography to track structural and physiological phenology in Mediterranean tree-grass ecosystems. *Remote Sensing*, 10(8), 1293. <https://doi.org/10.3390/rs10081293>
- Magney, T. S., Frankenberg, C., Fisher, J. B., Sun, Y., North, G. B., Davis, T. S., et al. (2017). Connecting active to passive fluorescence with photosynthesis: A method for evaluating remote sensing measurements of Chl fluorescence. *New Phytologist*, 215(4), 1594–1608. <https://doi.org/10.1111/nph.14662>
- Mahecha, M. D., Reichstein, M., Carvalhais, N., Lasslop, G., Lange, H., Seneviratne, S. I., et al. (2010). Global convergence in the temperature sensitivity of respiration at ecosystem level. *Science*, 329(5993), 838–840. <https://doi.org/10.1126/science.1189587>
- Mahecha, M. D., Reichstein, M., Jung, M., Seneviratne, S. I., Zaehle, S., Beer, C., et al. (2010). Comparing observations and process-based simulations of biosphere-atmosphere exchanges on multiple timescales. *Journal of Geophysical Research: Biogeosciences*, 115(2), 1–21. <https://doi.org/10.1029/2009JG001016>
- Mahecha, M. D., Reichstein, M., Lange, H., Carvalhais, N., Bernhofer, C., Grünwald, T., et al. (2007). Characterizing ecosystem-atmosphere interactions from short to interannual time scales. *Biogeosciences*, 4(5), 743–758. <https://doi.org/10.5194/bg-4-743-2007>
- Martín, M. P., Pacheco-Labrador, J., González-Cascón, R., Moreno, G., Migliavacca, M., García, M., et al. (2020). Estimation of essential vegetation variables in a dehesa ecosystem using reflectance factors simulated at different phenological stages. *Revista de Teledetección*, 55, 31. <https://doi.org/10.4995/raet.2020.13394>
- Martini, D., Pacheco-Labrador, J., Perez-Priego, O., van der Tol, C., El-Madany, T. S., Julitta, T., et al. (2019). Nitrogen and phosphorus effect on sun-induced fluorescence and gross primary productivity in mediterranean grassland. *Remote Sensing*, 11(21), 2562. <https://doi.org/10.3390/rs11212562>
- Melendo-Vega, J. R., Martín, M. P., Pacheco-Labrador, J., González-Cascón, R., Moreno, G., Pérez, F., et al. (2018). Improving the performance of 3-D radiative transfer model FLIGHT to simulate optical properties of a tree-grass ecosystem. *Remote Sensing*, 10(12), 2061. <https://doi.org/10.3390/rs10122061>
- Merlier, E., Hmimina, G., Dufrène, E., & Soudani, K. (2015). Explaining the variability of the photochemical reflectance index (PRI) at the canopy-scale: Disentangling the effects of phenological and physiological changes. *Journal of Photochemistry and Photobiology B: Biology*, 151, 161–171. <https://doi.org/10.1016/j.jphotobiol.2015.08.006>
- Meroni, M., Rossini, M., Guanter, L., Alonso, L., Rascher, U., Colombo, R., & Moreno, J. (2009). Remote sensing of solar-induced chlorophyll fluorescence: Review of methods and applications. *Remote Sensing of Environment*, 113(10), 2037–2051. <https://doi.org/10.1016/j.rse.2009.05.003>
- Middleton, E. M., Huemmrich, K. F., Landis, D. R., Black, T. A., Barr, A. G., & McCaughey, J. H. (2016). Photosynthetic efficiency of northern forest ecosystems using a MODIS-derived photochemical reflectance index (PRI). *Remote Sensing of Environment*, 187, 345–366. <https://doi.org/10.1016/j.rse.2016.10.021>
- Middleton, E. M., Rascher, U., Corp, L. A., Huemmrich, K. F., Cook, B. D., Noormets, A., et al. (2017). The 2013 FLEX-US airborne campaign at the parker tract loblolly pine plantation in North Carolina, USA. *Remote Sensing*, 9(6), 1–31. <https://doi.org/10.3390/rs9060612>
- Migliavacca, M., Perez-Priego, O., Rossini, M., El-Madany, T. S., Moreno, G., van der Tol, C., et al. (2017). Plant functional traits and canopy structure control the relationship between photosynthetic CO₂ uptake and far-red sun-induced fluorescence in a Mediterranean grassland under different nutrient availability. *New Phytologist*, 214(3), 1078–1091. <https://doi.org/10.1111/nph.14437>
- Migliavacca, M., Reichstein, M., Richardson, A. D., Mahecha, M. D., Cremonese, E., Delpierre, N., et al. (2015). Influence of physiological phenology on the seasonal pattern of ecosystem respiration in deciduous forests. *Global Change Biology*, 21(1), 363–376. <https://doi.org/10.1111/gcb.12671>
- Mohammed, G. H., Colombo, R., Middleton, E. M., Rascher, U., van der Tol, C., Nedbal, L., et al. (2019). Remote sensing of solar-induced chlorophyll fluorescence (SIF) in vegetation: 50 years of progress. *Remote Sensing of Environment*, 231, 111177. <https://doi.org/10.1016/j.rse.2019.04.030>
- Monteith, J. L. (1972). Solar radiation and productivity in tropical ecosystems. *The Journal of Applied Ecology*, 9(3), 747. <https://doi.org/10.2307/2401901>
- Müller, P., Li, X. P., & Niyogi, K. K. (2001). Non-photochemical quenching. A response to excess light energy. *Plant Physiology*, 125(4), 1558–1566. <https://doi.org/10.1104/pp.125.4.1558>
- Nelson, J. A., Carvalhais, N., Cuntz, M., Delpierre, N., Knauer, J., Ogée, J., et al. (2018). Coupling water and carbon fluxes to constrain estimates of transpiration: The TEA algorithm. *Journal of Geophysical Research: Biogeosciences*, 123(12), 3617–3632. <https://doi.org/10.1029/2018JG004727>

- Niyogi, K. K., Björkman, O., & Grossman, A. R. (1997). The roles of specific xanthophylls in photoprotection. *Proceedings of the National Academy of Sciences of the United States of America*, *94*(25), 14162–14167. <https://doi.org/10.1073/pnas.94.25.14162>
- Pacheco-Labrador, J., Perez-Priego, O., El-Madany, T. S., Julitta, T., Rossini, M., Guan, J., et al. (2019). Multiple-constraint inversion of SCOPE. Evaluating the potential of GPP and SIF for the retrieval of plant functional traits. *Remote Sensing of Environment*, *234*, 111362. <https://doi.org/10.1016/j.rse.2019.111362>
- Perez-Priego, O., El-Madany, T. S., Migliavaca, M., Kowalski, A. S., Jung, M., Carrara, A., et al. (2017). Evaluation of eddy covariance latent heat fluxes with independent lysimeter and sapflow estimates in a Mediterranean savannah ecosystem. *Agricultural and Forest Meteorology*, *236*, 87–99. <https://doi.org/10.1016/j.agrformet.2017.01.009>
- Perez-Priego, O., Guan, J., Rossini, M., Fava, F., Wutzler, T., Moreno, G., et al. (2015). Sun-induced chlorophyll fluorescence and photochemical reflectance index improve remote-sensing gross primary production estimates under varying nutrient availability in a typical Mediterranean savanna ecosystem. *Biogeosciences*, *12*(21), 6351–6367. <https://doi.org/10.5194/bg-12-6351-2015>
- Pfündel, E., & Bilger, W. (1994). Regulation and possible function of the violaxanthin cycle. *Photosynthesis Research*, *42*(2), 89–109. <https://doi.org/10.1007/BF02187121>
- Plaut, G., Ghil, M., & Vautard, R. (1995). Interannual and interdecadal variability in 335 years of central England temperatures. *Science*, *268*(5211), 710–713. <https://doi.org/10.1126/science.268.5211.710>
- Porcar-Castell, A. (2011). A high-resolution portrait of the annual dynamics of photochemical and non-photochemical quenching in needles of *Pinus sylvestris*. *Physiologia Plantarum*, *143*(2), 139–153. <https://doi.org/10.1111/j.1399-3054.2011.01488.x>
- Porcar-Castell, A., Mac Arthur, A., Rossini, M., Eklundh, L., Pacheco-Labrador, J., Anderson, K., et al. (2015). EUROSPEC: At the interface between remote-sensing and ecosystem CO₂ flux measurements in Europe. *Biogeosciences*, *12*(20), 6103–6124. <https://doi.org/10.5194/bg-12-6103-2015>
- Porcar-Castell, A., Pfündel, E., Korhonen, J. F. J., & Juurola, E. (2008). A new monitoring PAM fluorometer (MONI-PAM) to study the short- and long-term acclimation of photosystem II in field conditions. *Photosynthesis Research*, *96*(2), 173–179. <https://doi.org/10.1007/s1120-008-9292-3>
- Porcar-Castell, A., Tyystjärvi, E., Atherton, J., van der Tol, C., Flexas, J., Pfündel, E. E., et al. (2014). Linking chlorophyll a fluorescence to photosynthesis for remote sensing applications: Mechanisms and challenges. *Journal of Experimental Botany*, *65*(15), 4065–4095. <https://doi.org/10.1093/jxb/eru191>
- Rascher, U., Alonso, L., Burkart, A., Cilia, C., Cogliati, S., Colombo, R., et al. (2015). Sun-induced fluorescence - A new probe of photosynthesis: First maps from the imaging spectrometer HyPlant. *Global Change Biology*, *21*(12), 4673–4684. <https://doi.org/10.1111/gcb.13017>
- Rebmann, C., Aubinet, M., Schmid, H., Arriga, N., Aurela, M., Burba, G., et al. (2018). ICOS eddy covariance flux-station site setup: A review. *International Agrophysics*, *32*(4), 471–494. <https://doi.org/10.1515/intag-2017-0044>
- Reda, I., & Andreas, A. (2004). Solar position algorithm for solar radiation applications. *Solar Energy*, *76*(5), 577–589. <https://doi.org/10.1016/j.solener.2003.12.003>
- Reichstein, M., Falge, E., Baldocchi, D., Papale, D., Aubinet, M., Berbigier, P., et al. (2005). On the separation of net ecosystem exchange into assimilation and ecosystem respiration: Review and improved algorithm. *Global Change Biology*, *11*(9), 1424–1439. <https://doi.org/10.1111/j.1365-2486.2005.001002.x>
- Rossini, M., Nedbal, L., Guanter, L., Ač, A., Alonso, L., Burkart, A., et al. (2015). Red and far red Sun-induced chlorophyll fluorescence as a measure of plant photosynthesis. *Geophysical Research Letters*, *42*(6), 1632–1639. <https://doi.org/10.1002/2014GL062943>
- Serrano, L., Gamon, J. A., & Penuelas, J. (2000). Estimation of canopy photosynthetic and nonphotosynthetic components from spectral transmittance. *Ecology*, *81*(11), 3149–3162. [https://doi.org/10.1890/0012-9658\(2000\)081\[3149:EOCPAN\]2.0.CO;2](https://doi.org/10.1890/0012-9658(2000)081[3149:EOCPAN]2.0.CO;2)
- Siegmann, B., Cendrero-Mateo, M. P., Cogliati, S., Damm, A., Gamon, J., Herrera, D., et al. (2021). Downscaling of far-red solar-induced chlorophyll fluorescence of different crops from canopy to leaf level using a diurnal data set acquired by the airborne imaging spectrometer HyPlant. *Remote Sensing of Environment*, *264*, 112609. <https://doi.org/10.1016/j.rse.2021.112609>
- Sims, D. A., & Gamon, J. A. (2002). Relationships between leaf pigment content and spectral reflectance across a wide range of species, leaf structures and developmental stages. *Remote Sensing of Environment*, *81*(2–3), 337–354. [https://doi.org/10.1016/S0034-4257\(02\)00010-X](https://doi.org/10.1016/S0034-4257(02)00010-X)
- Sun, Y., Frankenberg, C., Jung, M., Joiner, J., Guanter, L., Köhler, P., & Magney, T. (2018). Overview of solar-induced chlorophyll fluorescence (SIF) from the orbiting carbon observatory-2: Retrieval, cross-mission comparison, and global monitoring for GPP. *Remote Sensing of Environment*, *209*, 808–823. <https://doi.org/10.1016/j.rse.2018.02.016>
- Tagliabue, G., Panigada, C., Dechant, B., Baret, F., Cogliati, S., Colombo, R., et al. (2019). Exploring the spatial relationship between airborne-derived red and far-red sun-induced fluorescence and process-based GPP estimates in a forest ecosystem. *Remote Sensing of Environment*, *231*, 111272. <https://doi.org/10.1016/j.rse.2019.111272>
- Tucker, C. J. (1979). Red and photographic infrared linear combinations for monitoring vegetation. *Remote Sensing of Environment*, *8*(2), 127–150. [https://doi.org/10.1016/0034-4257\(79\)90013-0](https://doi.org/10.1016/0034-4257(79)90013-0)
- van der Tol, C., Berry, J. A., Campbell, P. K. E., & Rascher, U. (2014). Models of fluorescence and photosynthesis for interpreting measurements of solar-induced chlorophyll fluorescence. *Journal of Geophysical Research: Biogeosciences*, *119*(12), 2312–2327. <https://doi.org/10.1002/2014JG002713>
- van der Tol, C., Verhoef, W., Timmermans, J., Verhoef, A., & Su, Z. (2009). An integrated model of soil-canopy spectral radiance observations, photosynthesis, fluorescence, temperature and energy balance. *Biogeosciences Discussions*, *6*(3), 6025–6075. <https://doi.org/10.5194/bgd-6-6025-2009>
- Verhoef, W., van der Tol, C., & Middleton, E. M. (2018). Hyperspectral radiative transfer modeling to explore the combined retrieval of biophysical parameters and canopy fluorescence from FLEX - Sentinel-3 tandem mission multi-sensor data. *Remote Sensing of Environment*, *204*, 942–963. <https://doi.org/10.1016/j.rse.2017.08.006>
- Vilfan, N., van der Tol, C., Muller, O., Rascher, U., & Verhoef, W. (2016). Fluspect-B: A model for leaf fluorescence, reflectance and transmittance spectra. *Remote Sensing of Environment*, *186*, 596–615. <https://doi.org/10.1016/j.rse.2016.09.017>
- Vilfan, N., van der Tol, C., Yang, P., Wyber, R., Malenovsky, Z., Robinson, S. A., & Verhoef, W. (2018). Extending fluspect to simulate xanthophyll driven leaf reflectance dynamics. *Remote Sensing of Environment*, *211*, 345–356. <https://doi.org/10.1016/j.rse.2018.04.012>
- Wang, T., Brender, P., Ciaia, P., Piao, S., Mahecha, M. D., Chevallier, F., et al. (2012). State-dependent errors in a land surface model across biomes inferred from eddy covariance observations on multiple timescales. *Ecological Modelling*, *246*, 11–25. <https://doi.org/10.1016/j.ecolmodel.2012.07.017>
- Wang, X., Chen, J. M., & Ju, W. (2020). Photochemical reflectance index (PRI) can be used to improve the relationship between gross primary productivity (GPP) and sun-induced chlorophyll fluorescence (SIF). *Remote Sensing of Environment*, *246*, 111888. <https://doi.org/10.1016/J.RSE.2020.111888>

- Wieneke, S., Burkart, A., Cendrero-Mateo, M. P., Julitta, T., Rossini, M., Schickling, A., et al. (2018). Linking photosynthesis and sun-induced fluorescence at sub-daily to seasonal scales. *Remote Sensing of Environment*, *219*, 247–258. <https://doi.org/10.1016/j.rse.2018.10.019>
- Xu, S., Atherton, J., Riikonen, A., Zhang, C., Oivukkamäki, J., MacArthur, A., et al. (2021). Structural and photosynthetic dynamics mediate the response of SIF to water stress in a potato crop. *Remote Sensing of Environment*, *263*, 112555. <https://doi.org/10.1016/j.rse.2021.112555>
- Yamamoto, H. Y. (1979). Biochemistry of the violaxanthin cycle in higher plants. *Pure and Applied Chemistry*, *51*(3), 639–648. <https://doi.org/10.1351/pac197951030639>
- Yiou, P., Baert, E., & Loutre, M. F. (1996). Spectral analysis of climate data. *Surveys in Geophysics*, *17*(6), 619–663. <https://doi.org/10.1007/BF01931784>
- Zhang, Z., Zhang, Y., Porcar-Castell, A., Joiner, J., Guanter, L., Yang, X., et al. (2020). Reduction of structural impacts and distinction of photosynthetic pathways in a global estimation of GPP from space-borne solar-induced chlorophyll fluorescence. *Remote Sensing of Environment*, *240*, 111722. <https://doi.org/10.1016/j.rse.2020.111722>